

Supplementary Materials for

Varied Response of Western Pacific Hydrology to Climate Forcings over the Last Glacial Period

Stacy A. Carolin,* Kim M. Cobb, Jess F. Adkins, Brian Clark, Jessica L. Conroy, Syria Lejau, Jenny Malang, Andrew A. Tuen

*Corresponding author. E-mail: stacy.carolin@gatech.edu

Published 6 June 2012 on *Science* Express
DOI: 10.1126/science.1233797

This PDF file includes:

Materials and Methods
Figs. S1 to S12
Tables S1 to S4
Full Reference List

Supplementary Materials for**“Varied response of western Pacific hydrology to climate forcings over the last glacial period”****Supplementary Materials:**

Materials and Methods

Figures S1-S12

Tables S1-S4

References (36-38)

Methods and Materials*I. General Description of Stalagmites*

The four stalagmites were collected from Gunung Mulu and Gunung Buda National Parks (4°N, 115°E) (Fig. S1). SC02 and SC03 were recovered from Secret Cave at Gunung Mulu in 2006, SCH02 from Snail Shell Cave at Gunung Buda in 2003, and BA02 from Bukit Assam Cave at Gunung Buda in 2003. Borneo stalagmites are particularly difficult to date because they have relatively low ^{238}U concentrations, negative $\delta^{234}\text{U}$ values, and contain appreciable levels of detrital thorium. For this reason, we overlap four $\delta^{18}\text{O}$ records from separate stalagmites with different growth rates from caves 20 km apart in order to confirm reproducibility and robustness of the resulting composite oxygen isotopic record. 101 dates were measured across 4 stalagmites, of which 5 fell out of chronological order. 95 of the 101 dates have relative 2σ age errors less than 2.0%, and 77 dates have relative 2σ age errors less than 1.0%. The new Borneo $\delta^{18}\text{O}$ record is unique in that of the 85ky-period covered by the reconstruction, over 50ky are covered by 2 separate overlapping stalagmite records, 30ky by 3 overlapping stalagmite records, and 8ky by all 4 overlapping stalagmite records. As expected, comparing multiple $\delta^{18}\text{O}$ records for a given time period allows for a clear visual identification of age model errors associated with dating uncertainties. This is evident by comparing the timing of five major $\delta^{18}\text{O}$ excursions that are shared across all of the stalagmite $\delta^{18}\text{O}$. To correct for small offsets in the timing of such events between the individual stalagmite $\delta^{18}\text{O}$ records, we align these events across the four records within the 2σ age errors associated with each stalagmite age model. We also plot the original age model in Figure 1 of the main paper, which differs only slightly from the corrected age model (see Table S4). Our main conclusions are not dependent on the choice of raw versus aligned age models.

II. U-Series Age Model Construction

Age models were constructed for each stalagmite using U-series disequilibrium (^{238}U - ^{234}U - ^{230}Th) measurements with the isotopic compositions of the U and Th fractions determined with a Finnigan Neptune MC-ICPMS at Caltech (see Methods from Partin et al., 2007). We report measured [^{238}U], [^{232}Th], $\delta^{234}\text{U}$, and ($^{230}\text{Th}/^{238}\text{U}$)_A in Table S1 for all samples. The Secret Cave samples (SC03 and SC02) have the lowest ^{238}U and detrital Th concentrations, and the measured $\delta^{234}\text{U}$ ratios are negative and close to zero ($^{234}\text{U}/^{238}\text{U}$ activity closer to secular

equilibrium). The Snail Shell Cave (SCH02) and Bukit Assam Cave (BA02) samples have greater ^{238}U and detrital Th concentrations, with more depleted measured $\delta^{234}\text{U}$ ratios. A triple isotope plot (Figure S10), which graphically displays the range of $\delta^{234}\text{U}$ and $^{230}\text{Th}/^{238}\text{U}$ values for each stalagmite, shows that sample BA02 is particularly difficult to date as its initial $\delta^{234}\text{U}$ values place it close to the infinite age line.

A. Calculating Detrital $^{230}\text{Th}/^{232}\text{Th}$ Contamination

We analyzed seven isochrons for this study, which are added to the 4 isochrons previously published for stalagmites from Bukit Assam cave and 3 isochrons previously published for stalagmites from Snail Shell cave (see Partin et al., 2007). The isotopic ratios used to create Osmond Type-II isochrons, ($^{232}\text{Th}/^{238}\text{U}$)_A, ($^{230}\text{Th}/^{238}\text{U}$)_A, and ($^{234}\text{U}/^{238}\text{U}$)_A, and their associated analytical 2σ errors are provided in Table S2. Osmond Type-II diagrams were used to determine detrital $^{230}\text{Th}/^{232}\text{Th}$ concentrations because normalizing to ^{238}U makes deviation from a linear fit much more evident than normalizing to ^{232}Th (36). We implemented ISOPLOT 3.72 (37) to calculate the detrital $^{230}\text{Th}/^{232}\text{Th}$ concentration, which utilizes a maximum-likelihood estimation (MLE) XY-XZ isochron algorithm and a simple ^{232}Th correction algorithm (36). These algorithms simultaneously determine the best fit to a set of XY ($^{230}\text{Th}/^{238}\text{U}$ - $^{232}\text{Th}/^{238}\text{U}$) points and a set of XZ ($^{234}\text{Th}/^{238}\text{U}$ - $^{232}\text{Th}/^{238}\text{U}$) points. Error ellipses in the XY-XZ isochron diagrams are dominated by ^{234}U , ^{230}Th , and ^{232}Th measurement uncertainties. However, it is almost always the degree of scatter of points about a line, coupled to the spread of the data points along the axes (rather than the analytical error bars), that determines the uncertainty in the initial $^{230}\text{Th}/^{232}\text{Th}$ ratio. All isochrons for each cave system are plotted on the same Osmond Type-II plot in Figure S11. The age, planar intercepts, and detrital $^{230}\text{Th}/^{232}\text{Th}$ concentrations for each isochron calculated using the ISOPLOT 3.72 program are provided in Table S3, along with uncertainties.

The large scatter of $^{230}\text{Th}/^{232}\text{Th}$ values from the individual isochrons (Table S3) is an indication that more than one source of initial ^{230}Th exists in our system and motivates us to take a conservative approach (i.e. larger error bars) to estimating a detrital $^{230}\text{Th}/^{232}\text{Th}$ ratio that is representative of our cave system. The weighted means and standard deviations for the detrital $^{230}\text{Th}/^{232}\text{Th}$ concentration are calculated for each stalagmite using the inverse of the 1σ errors from each isochron as the weighting factor (Table S3). The weighted standard deviation is equal to the inverse of the sum of the weights for each cave system. Un-weighted means and standard deviations (for the population of isochron results from the same stalagmite) are also calculated for comparison. There is a large difference between the weighted standard deviation and the spread of the initial values from each line (the “un-weighted standard deviation”). For the final estimate of the detrital $^{230}\text{Th}/^{232}\text{Th}$ ratio we use the calculated weighted means and an uncertainty that lies between the simple population spread and the weighted uncertainty (Fig. S12). The final 2σ uncertainty was chosen so that (a) it overlaps the mean $^{230}\text{Th}/^{232}\text{Th}$ calculated from isochrons with 2σ error bars less than 10 ppm and (b) it overlaps the 2σ uncertainty of the mean $^{230}\text{Th}/^{232}\text{Th}$ calculated from isochrons with 2σ error bars greater than 10 ppm. We assign detrital atomic $^{230}\text{Th}/^{232}\text{Th}$ ratios as follows: BA02 = 56 ± 11 ppm; SCH02 = 59 ± 13 ppm; SC03 and SC02 = 111 ± 41 ppm (2σ errors; Fig. S12). These ratios are greater than the typical detrital bulk earth ratio (4 ± 2 ppm 2σ) frequently used in other stalagmite U-series dating applications. The greater detrital atomic $^{230}\text{Th}/^{232}\text{Th}$ ratio is likely due to the lack of other source rocks besides the

Melinau Limestone in the Buda and Mulu cave. Our sampling site is essentially a rainforest draped over limestone with no other mineral sources of U or Th.

B. Final U-series Age Models

Table S1 lists the measured ^{238}U and ^{232}Th concentrations, the initial $\delta^{234}\text{U}$ ratios, and the $^{230}\text{Th}/^{238}\text{U}$ activity ratios for all 101 samples drilled for U-series dating. The reported ages and their 2σ uncertainties were estimated using a Monte Carlo technique that accounts for the errors in all isotope ratios and the uncertainty in the initial $^{230}\text{Th}/^{232}\text{Th}$ ratio. Analytical error contributions from $(^{230}\text{Th}/^{238}\text{U})_A$ and $\delta^{234}\text{U}$ measurements are typically much smaller than error contributions due to uncertainty in the calculated detrital $^{230}\text{Th}/^{232}\text{Th}$. If the relative age error is greater than 2% of the calculated age, the date is not used in constructing a stalagmite age model. Also, if a repeat dating sample was drilled directly above or below a previously analyzed sample, the date with the lower age error is used in the construction of a preliminary age model. Finally, the StalAge algorithm (9) is used to determine if any additional U-series dates should be discarded as outliers. If a U-series date falls outside the StalAge model's 95% confidence interval, it is withheld from the final age model. The dates that are withheld from the final age model construction (as well as all isochron samples excluding the sample from each isochrons line with the smallest age error) are listed in Table S1 in red (blue for an isochron's data point). An age model was then constructed by linearly interpolating between consecutive ages. Our linearly interpolated model falls within the StalAge 95% confidence intervals for most of the record (Figure S3-S6).

1. Hiatus detection

A high-resolution scanned image of each stalagmite and the corresponding backlit image reveal intervals of clear calcite (light) interrupted by detrital-contaminated calcite (dark) (Figures S3-S6). The beginning and ending of inferred hiatuses are indicated with colored arrows on the age-depth plots. Most potential hiatuses are identified in the stalagmite slab from optical evidence of a cessation of the carbonate accumulation (dark or white layer), and by U-series ages drilled immediately above and below such layers. Additional hiatuses were inferred wherever growth rates dropped below 10 $\mu\text{m}/\text{yr}$ in Bukat Assam or Snail Shell stalagmites (average growth rate $\sim 17 \mu\text{m}/\text{yr}$) or 3 $\mu\text{m}/\text{yr}$ in Secret Cave stalagmites (average growth rate $\sim 5 \mu\text{m}/\text{yr}$). Any $\delta^{18}\text{O}$ samples that fall on a potential hiatus were removed from the final oxygen isotope time series, as they are associated with large dating uncertainties. In the cases where hiatuses are inferred from dramatic changes in growth rate between two U-series dates, and where the culprit hiatus is visible as a narrow band visible in the stalagmite images, growth rates from adjacent dates were linearly interpolated to the hiatus layer from both sides (see Partin et al., 2007; see Fig. S3-6).

2. Alignment of major features in the stalagmite $\delta^{18}\text{O}$ records

Because all four stalagmite samples were collected from caves within 20 km of each other we assume that large millennial-scale $\delta^{18}\text{O}$ excursions that are shared between the overlapping $\delta^{18}\text{O}$ records reflect contemporaneous climate events. We have thus adjusted the ages of those samples that have greater detrital contamination to the best-constrained age model in a given interval, to within 2σ dating errors, so that in the five major millennial-scale $\delta^{18}\text{O}$ excursions that are shared among the four records are aligned. The final “wiggle-matched” age model depths and ages for each stalagmite are provided in Table S4, which shows that the “wiggle-matched” dates fall within the 2σ age errors of the U-series dates.

As evident in Figure 1 and S8, the $\delta^{18}\text{O}$ maximum in SCH02 at ~40kybp occurs roughly 1000 years earlier than the corresponding $\delta^{18}\text{O}$ maxima in the other three stalagmites, even after shifting the SCH02 age tie points to the extent allowed by the 2σ dating errors. In general, SCH02 contains more detrital material and a larger number of visible hiatuses (some resolved by U/Th dates and some that are likely too small to be detected) than the other stalagmites (Figure S5). As such, we feel more confident in the age assignments from the other three stalagmites at the ~40kybp interval, as they agree remarkably well.

III. Stable isotope measurements

Oxygen isotopic analyses were conducted on powders drilled every 0.5mm or 1mm along the central growth axis of the stalagmites with a 1.6 mm drill bit. The $\delta^{18}\text{O}$ were analyzed on a Finnigan 253 equipped with a Kiel device at Georgia Tech (long-term reproducibility of less than $\pm 0.07\text{\textperthousand}$ (1σ)). All $\delta^{18}\text{O}$ data are reported with respect to VPDB.

IV. Generation of a temperature-corrected sea level curve

Waelbroeck et al.'s (15) mean ocean $\delta^{18}\text{O}$ record derived from a temperature-corrected benthic $\delta^{18}\text{O}$ stack was used to adjust the Borneo $\delta^{18}\text{O}$ record to account for change in the mean $\delta^{18}\text{O}$ of seawater due to changes in ice volume. The derived mean ocean $\delta^{18}\text{O}$ record is plotted in Figure S7b. The individual stalagmite $\delta^{18}\text{O}$ records adjusted to account for the change in the $\delta^{18}\text{O}$ of the global ocean over the study interval are plotted in Figure S7c.

V. Calculation of Sunda Shelf areal exposure

An index tracking changes in the areal extent of the Sunda Shelf over the last glacial period was derived to determine how shelf exposure influenced hydroclimate variability in northern Borneo. Sunda shelf areal exposure was determined by converting the Waelbroeck et al.'s (15) derived sea level curve to relative areal shelf exposure using the NOAA ETOPO1 dataset of modern regional ocean bathymetry (<http://www.ngdc.noaa.gov/mgg/global/global.html>). In deriving our index of Sunda shelf area, we counted the number of 1x1 arc-minute grid boxes (1 minute of latitude = 1.853 km at the equator) exposed in an area defined as 95°E-120°E and 10°S-10°N with every 1m lowering of global sea level down to -130m. We then calculated the fraction of maximum Sunda shelf area exposure at each 1m interval. For example, if sea level is at -60m, then 452,048 grid boxes out of 611,208 Sunda shelf grid boxes are exposed, i.e. 74% of the Sunda shelf is above sea level. The resulting timeseries is plotted in brown in Figure S7d.

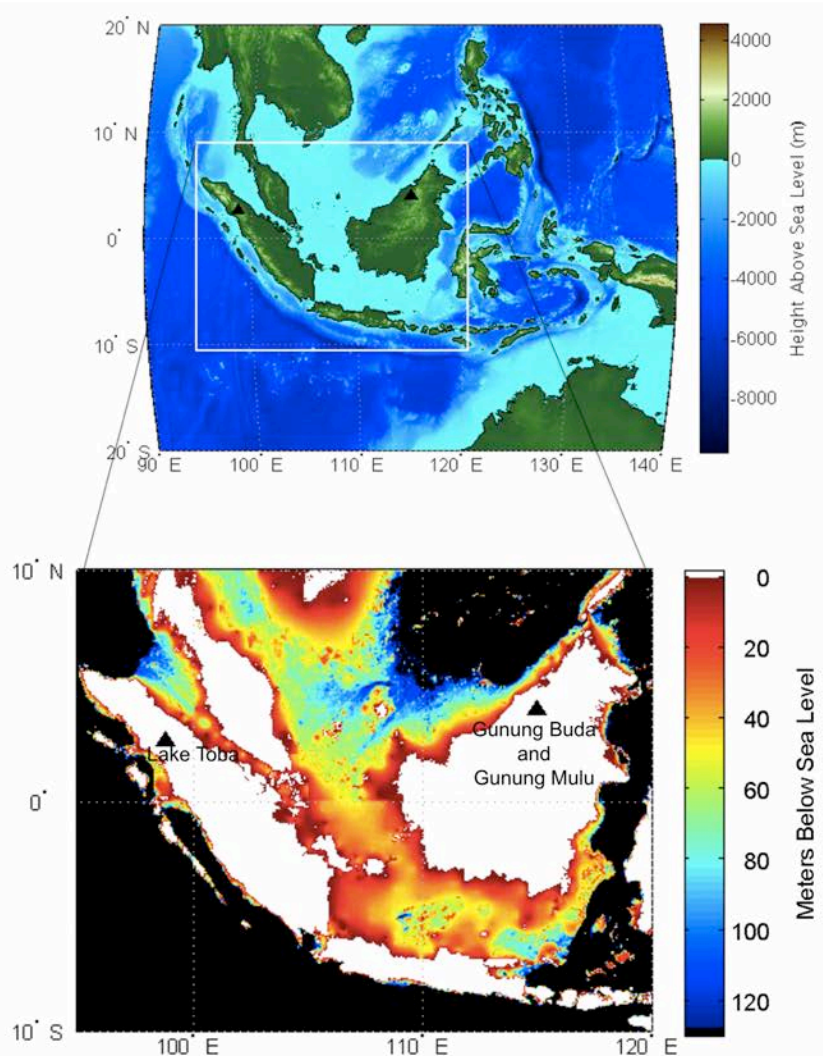


Figure S1. The location of Gunung Buda and Gunung Mulu National Parks relative to modern (top) and LGM (bottom) land/sea configurations. Topography and bathymetry provided in NOAA ETOP01 dataset (<http://www.ngdc.noaa.gov/mgg/global/global.html>).

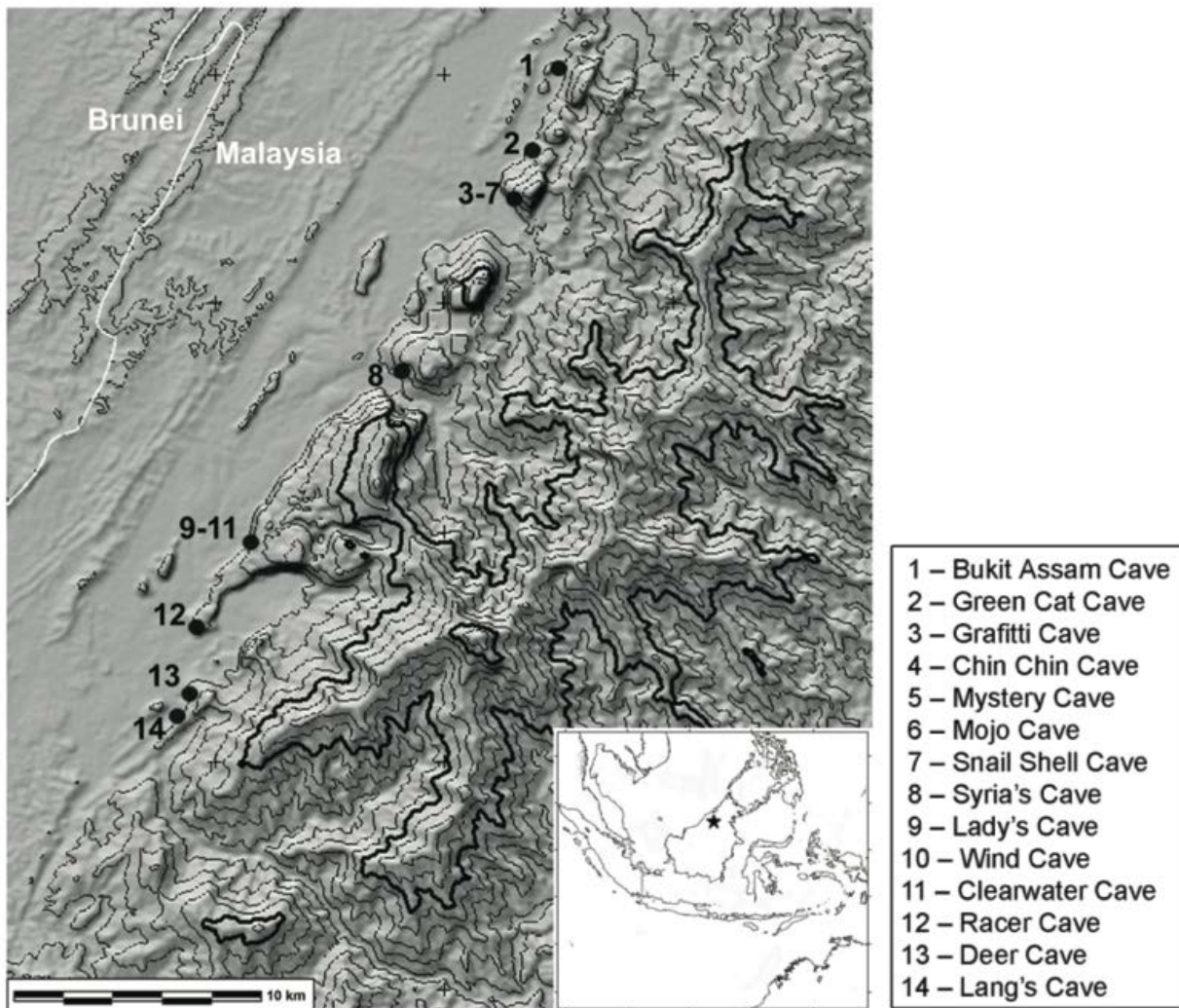


Figure S2: Topographic map of Gunung Mulu and Gunung Buda National Parks, Malaysia, showing cave locations (contour interval is 200m). Our new records come from Bukit Assam Cave (BA02), Snail Shell Cave (SCH02), and Secret Cave (SC02 and SC03; Secret is a chamber located inside Clearwater Cave). Topological data provided in SRTM30 (<http://www2.jpl.nasa.gov/srtm/>).

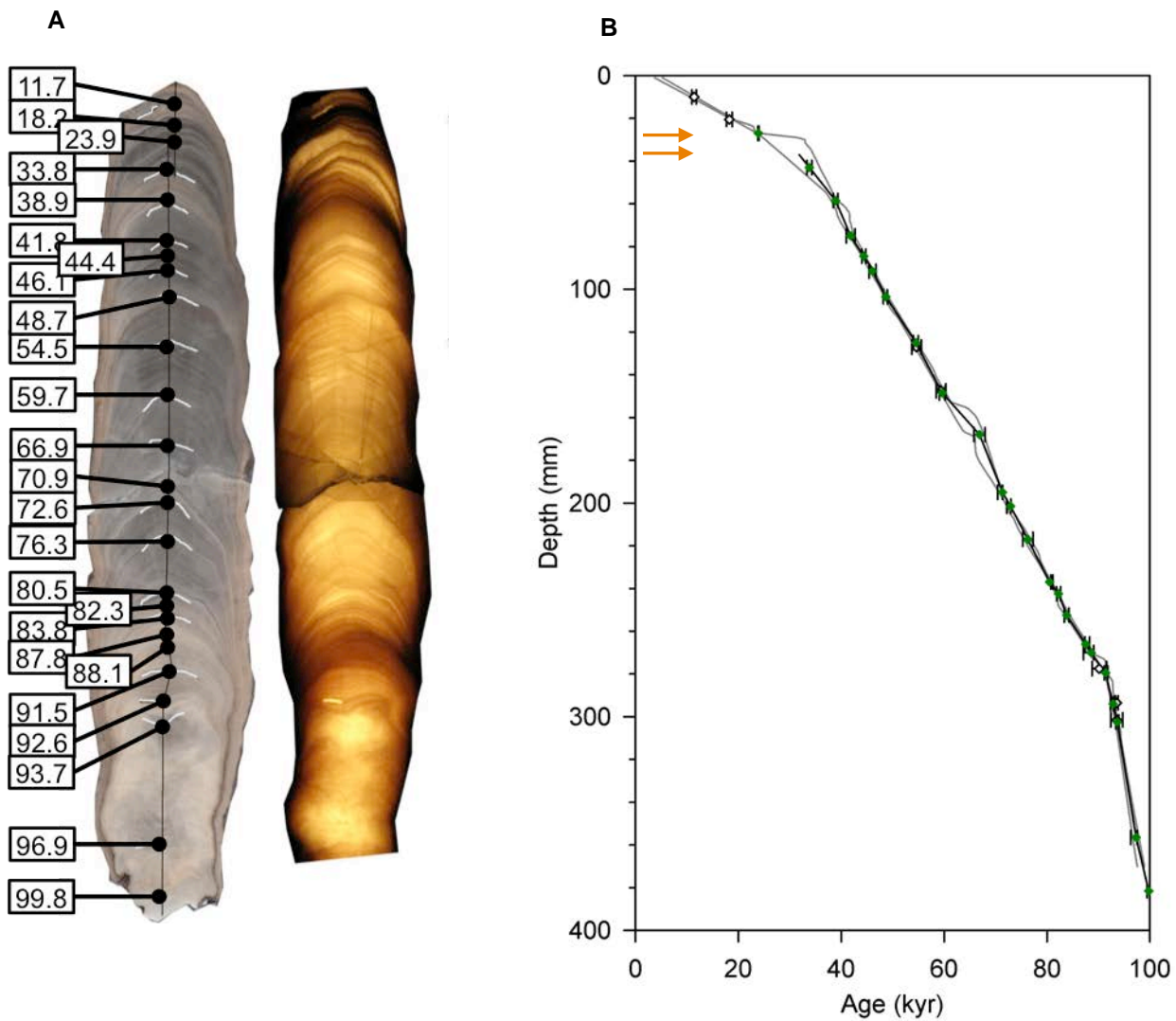


Figure S3. Reflected and backlit images for SC03 with its age versus depth plot. (A) High-resolution images of SC03, showing original U-series dates reported in kyr. Scale of photo matches y-axis scale used in age-depth plot in (B). (B) Age-depth plot for SC03. Data points in white are not included in age model (see Table S1). Data points in color are final ages used in age model (Table S4). Error bars represent 2σ dating uncertainties. Black line indicates our $\delta^{18}\text{O}$ -aligned age-depth model for SC03. Grey outer curves indicate 95% confidence interval endpoints for an ensemble of age models produced using StalAge (9). The duration of an identified hiatus is indicated by colored arrows.

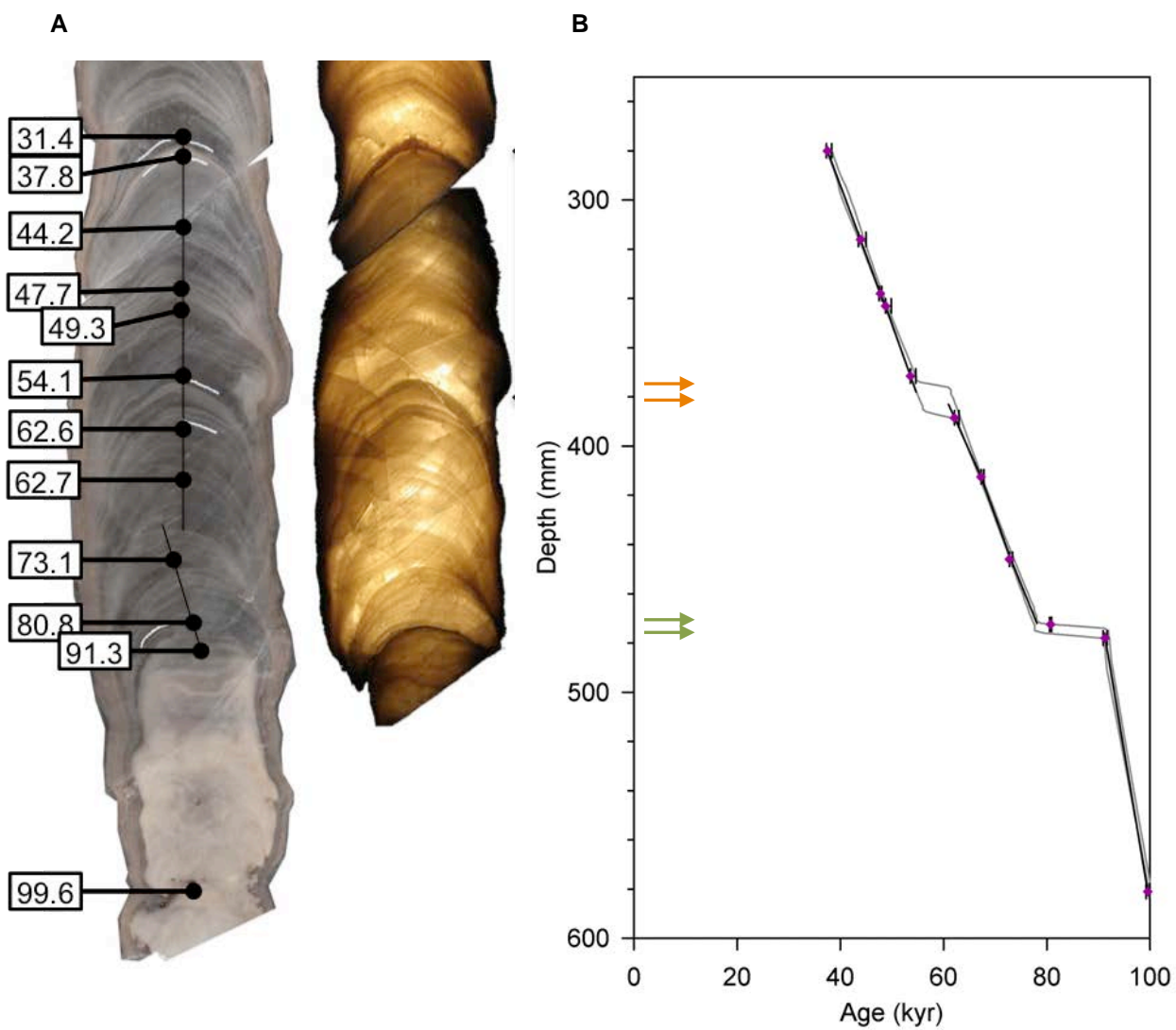


Figure S4. Same as Fig. S3 but for SC02. Two hiatuses are indicated.

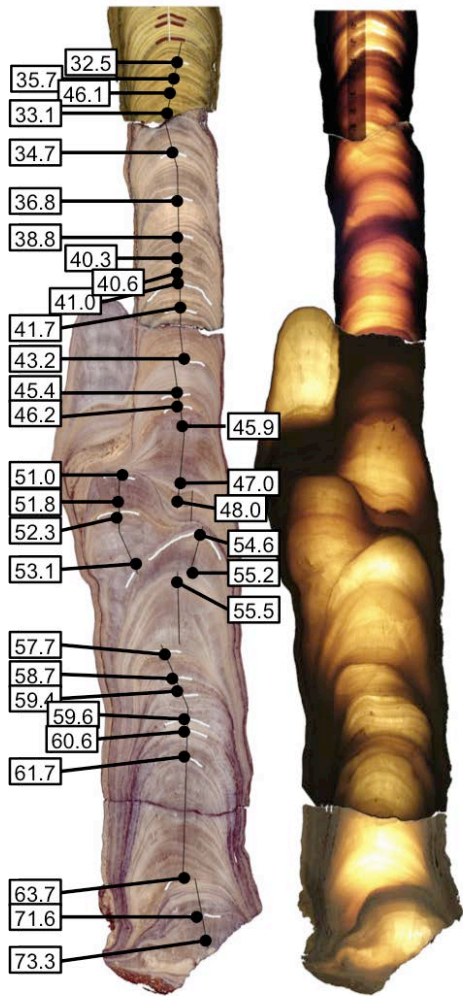
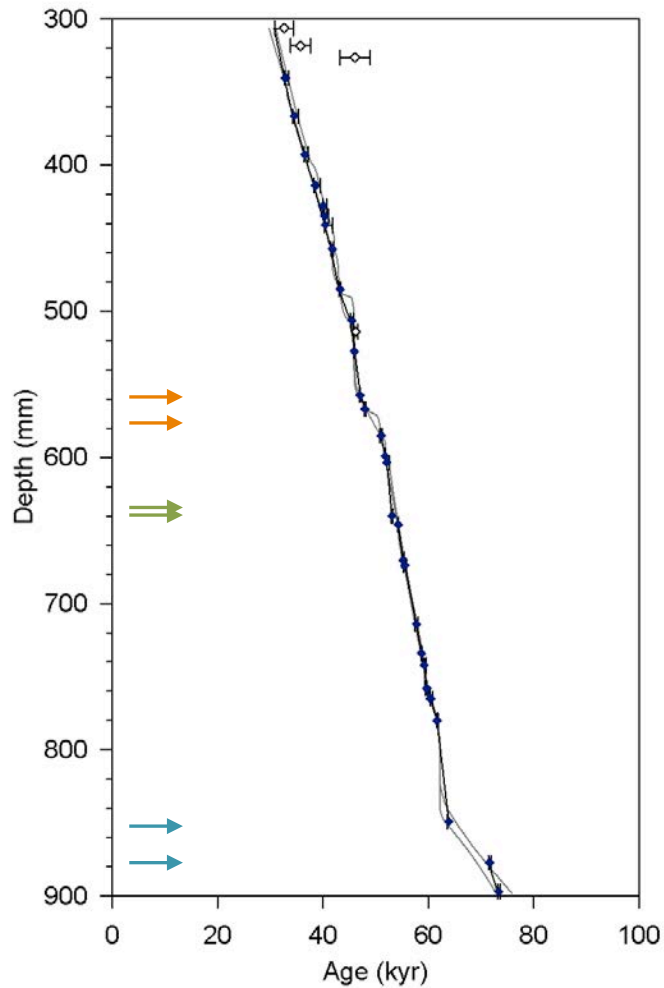
A**B**

Figure S5. Same as Fig. S3 but for SCH02. U-series dates from 0-30kyrp are previously published (Partin et al., 2007). Three hiatuses are indicated.

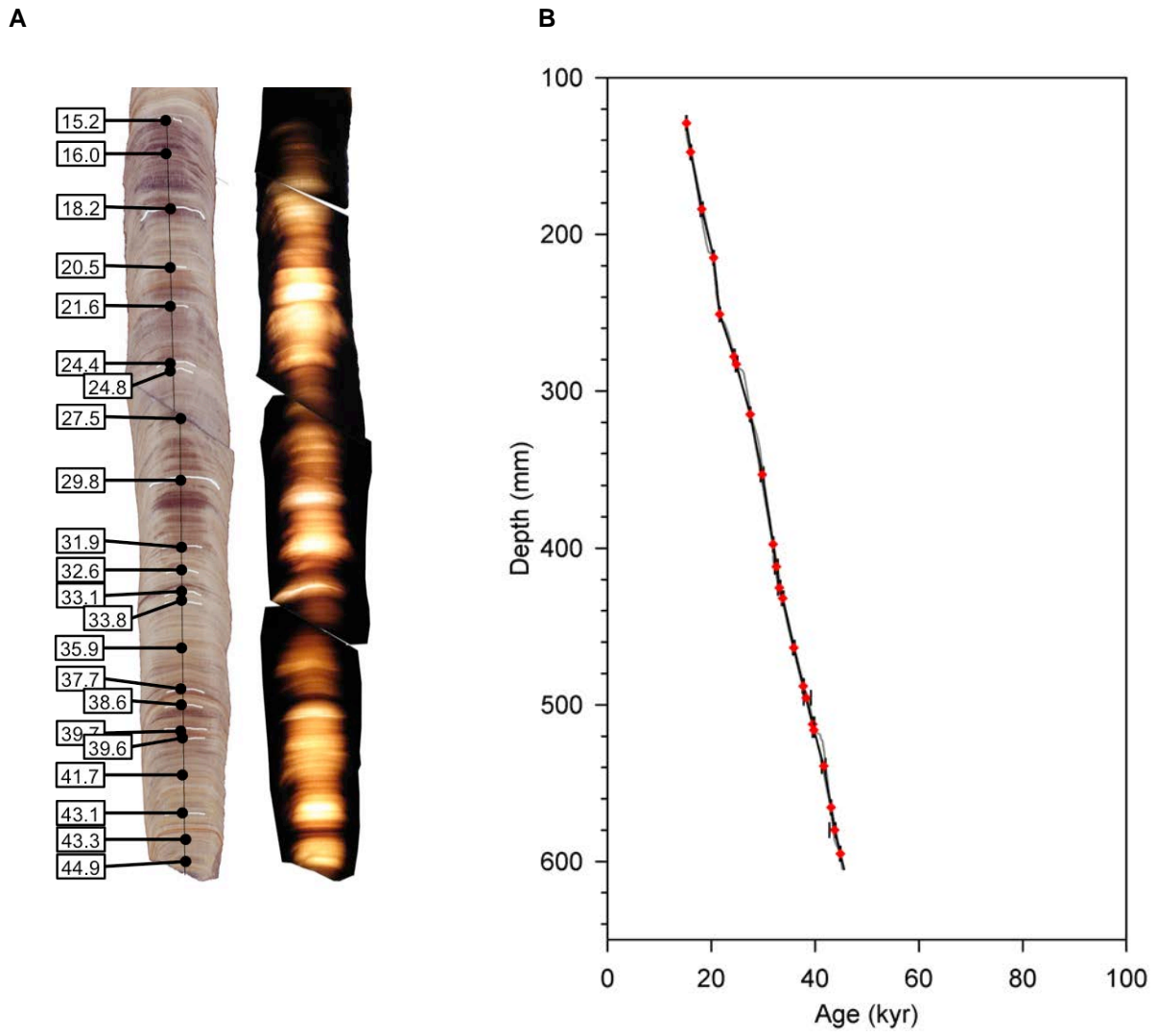


Figure S6. Same as Fig. S3 but for BA02. No hiatuses were found.

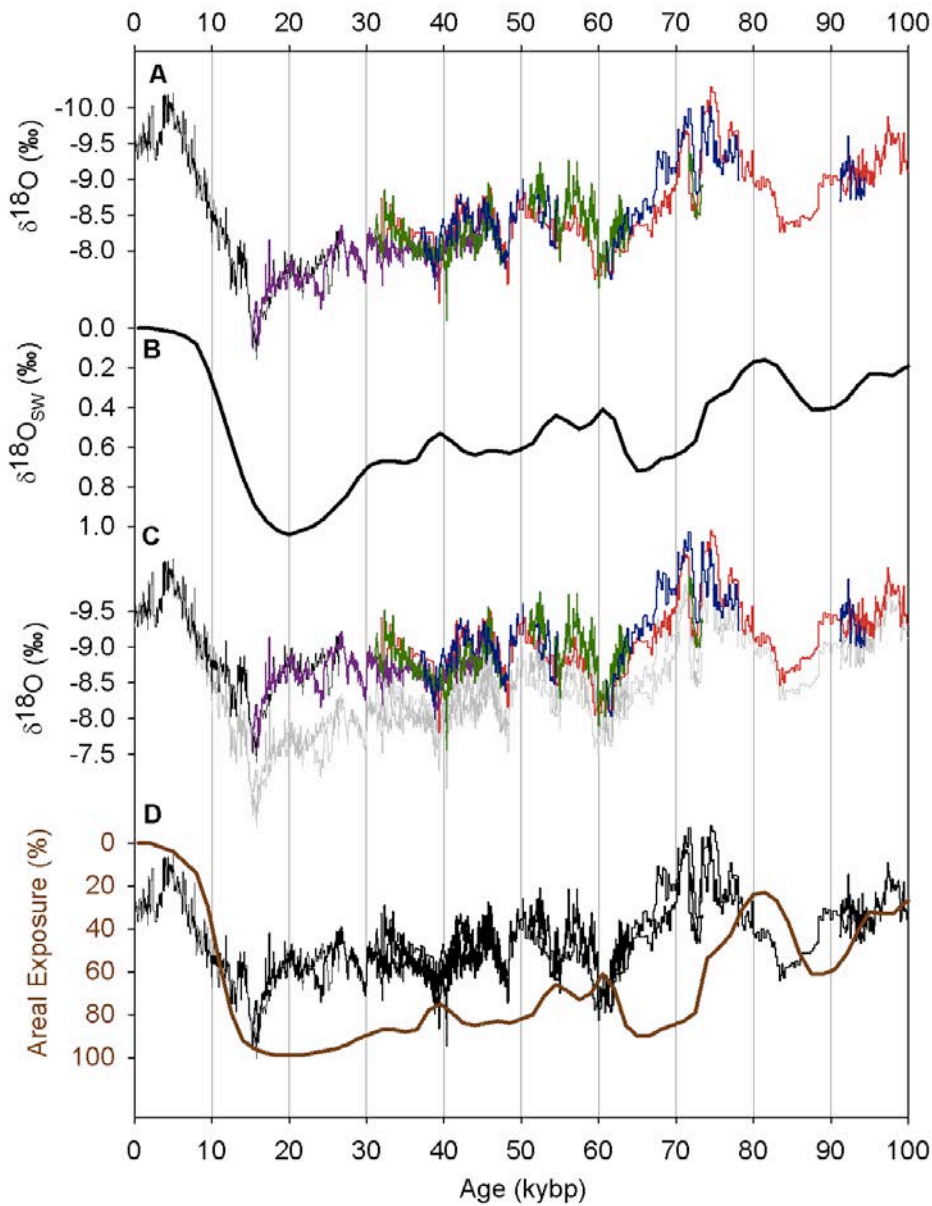


Figure S7. Timeseries of sea level and Sunda shelf areal exposure. **(A)** Borneo stalagmite $\delta^{18}\text{O}$ records. **(B)** Derived mean ocean $\delta^{18}\text{O}$ from temperature-adjusted benthic foraminifera stack (15). **(C)** The Borneo stalagmite $\delta^{18}\text{O}$ records after removing the influence of mean ocean $\delta^{18}\text{O}$ change due to ice volume (colors), plotted with the uncorrected Borneo stalagmite $\delta^{18}\text{O}$ records (grey). See Supplemental text for details. **(D)** Areal Sunda Shelf exposure extrapolated non-linearly from calculated sea level variability (brown), plotted with ice volume-corrected Borneo stalagmite $\delta^{18}\text{O}$ records from panel (C).

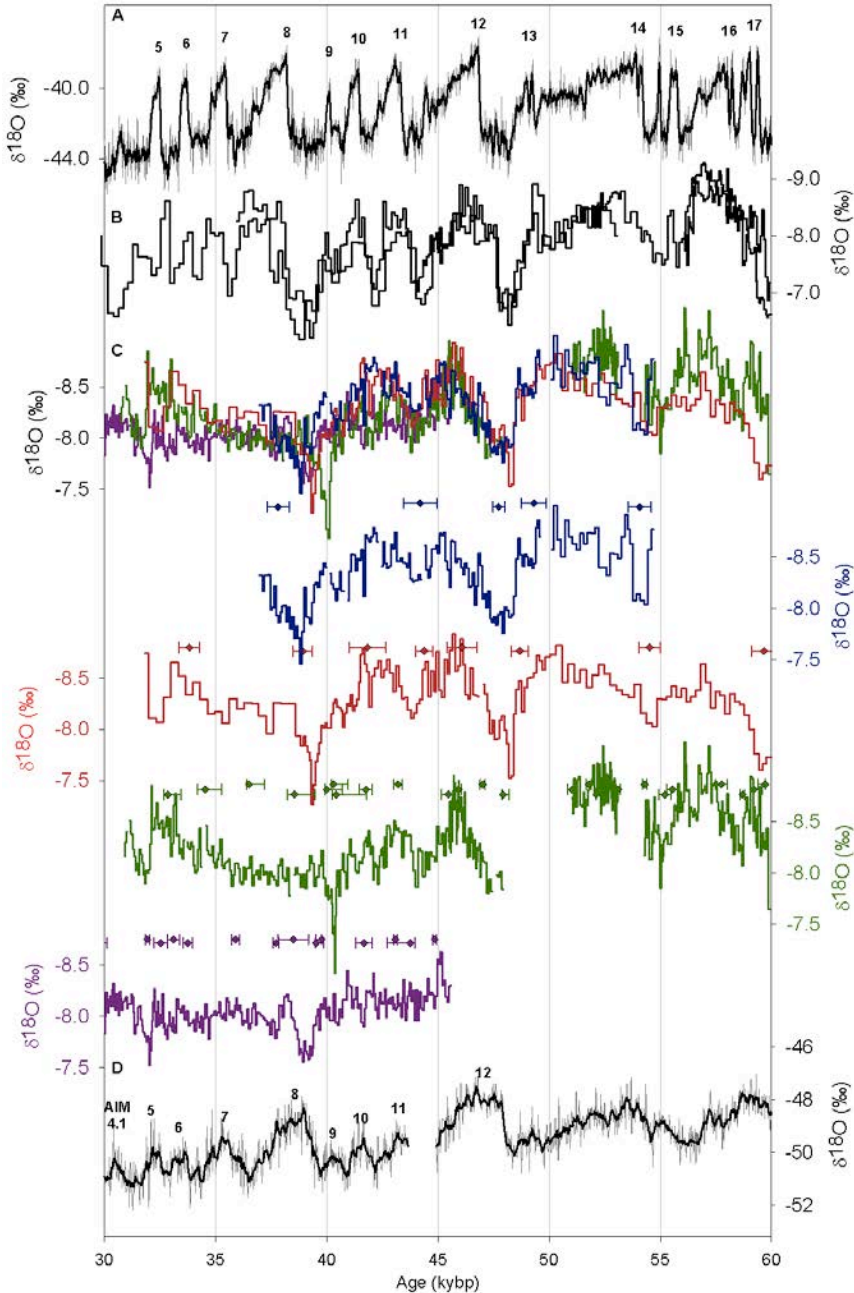


Figure S8. A detailed view of Stage 3 abrupt climate events as recorded in polar ice cores and in Chinese and Borneo stalagmite $\delta^{18}\text{O}$ records. **(A)** Greenland NGRIP ice core $\delta^{18}\text{O}$ (grey; 31) with 100yr averages (black), plotted using the GICC05modelext age model (32). Numbered D/O events are indicated. **(B)** Hulu/Sanbao cave stalagmite $\delta^{18}\text{O}$ records from China (1,2); The Sanbao $\delta^{18}\text{O}$ record has been offset by +1.6‰ for comparison. **(C)** The Borneo stalagmite $\delta^{18}\text{O}$ composite records and individual separated records: SC02 (navy), SC03 (red), SCH02 (green), BA02 (purple). U–Th dates used to construct age model used for the aligned composite record plotted in corresponding colors; error bars represent 2σ error (8). Raw U–Th dates are the midpoint of the plotted 2σ error bars, and are not shown. **(D)** EPICA Dronning Maud Land (EDML) ice core $\delta^{18}\text{O}$ (grey; 28) with 7-year averages (black). Antarctica Isotope Maxima (AIM) are indicated.

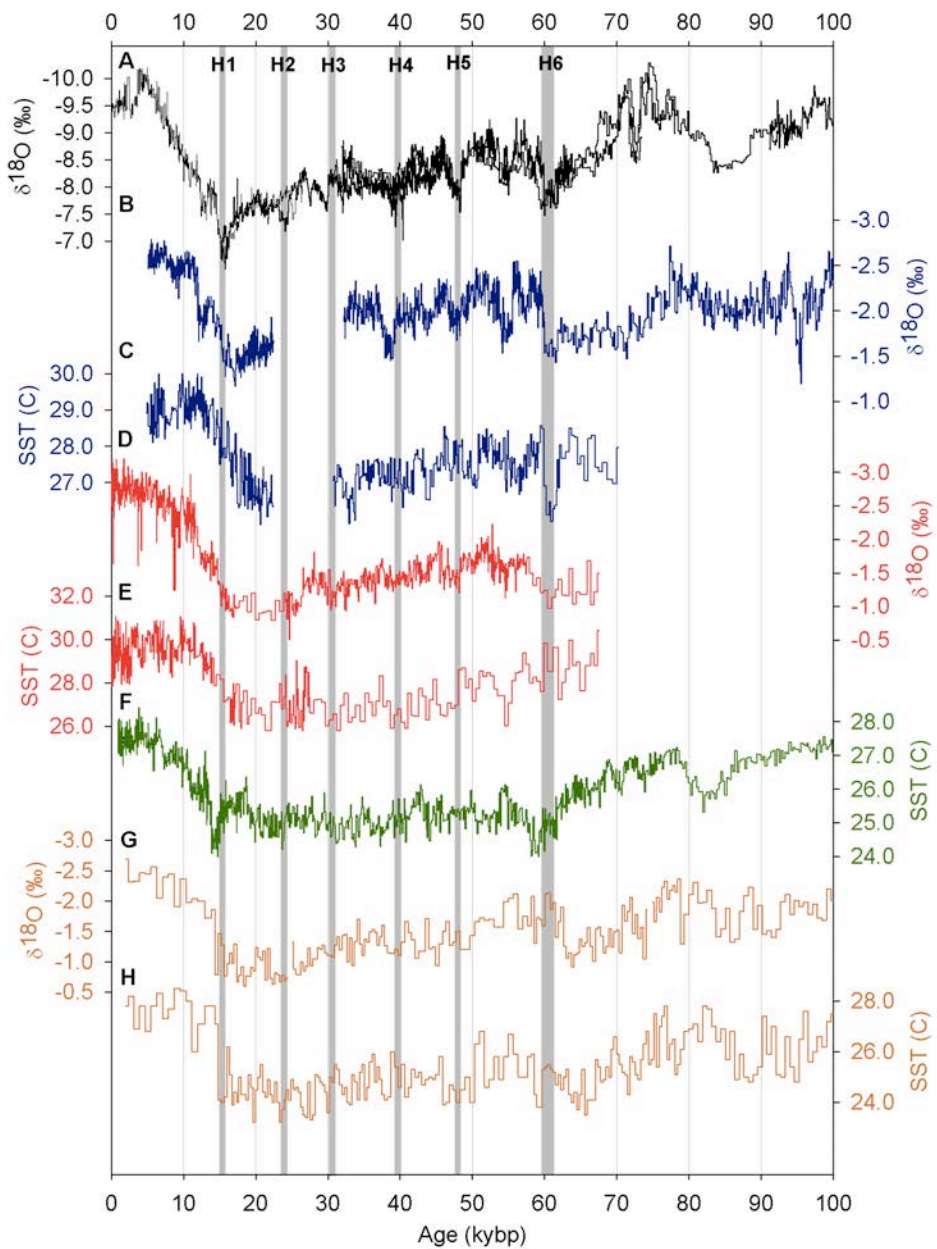


Figure S9. The Borneo stalagmite $\delta^{18}\text{O}$ records plotted with a variety of western tropical Pacific sediment core $\delta^{18}\text{O}$ and SST records. **(A)** Borneo stalagmite $\delta^{18}\text{O}$ records (uncorrected for ice volume). **(B)** Sulu Sea planktonic foraminifera $\delta^{18}\text{O}$ (24), plotted using an updated age model using IntCal09 calibration curve 41kybp-modern and aligning 60kybp $\delta^{18}\text{O}$ excursion to the Hulu/Sanbao stalagmite $\delta^{18}\text{O}$ records. **(C)** Sulu Sea planktonic foraminiferal Mg/Ca SST record (24), plotted using same updated age model as (B). **(D)** Site MD98-2181 planktonic foraminiferal $\delta^{18}\text{O}$ (38). **(E)** Site MD98-2181 planktonic foraminiferal Mg/Ca SST record (38). **(F)** South China Sea Site MD97-2151 UK'₃₇ SST (16). **(G)** South China Sea ODP Site 1145 planktonic foraminifera $\delta^{18}\text{O}$ (17). **(H)** ODP Site 1145 planktonic foraminifera Mg/Ca SST record (17). Grey vertical bars reflect the timing of Heinrich events H1-H6 (5) as recorded in the well-dated Chinese stalagmite $\delta^{18}\text{O}$ age models (1,2).

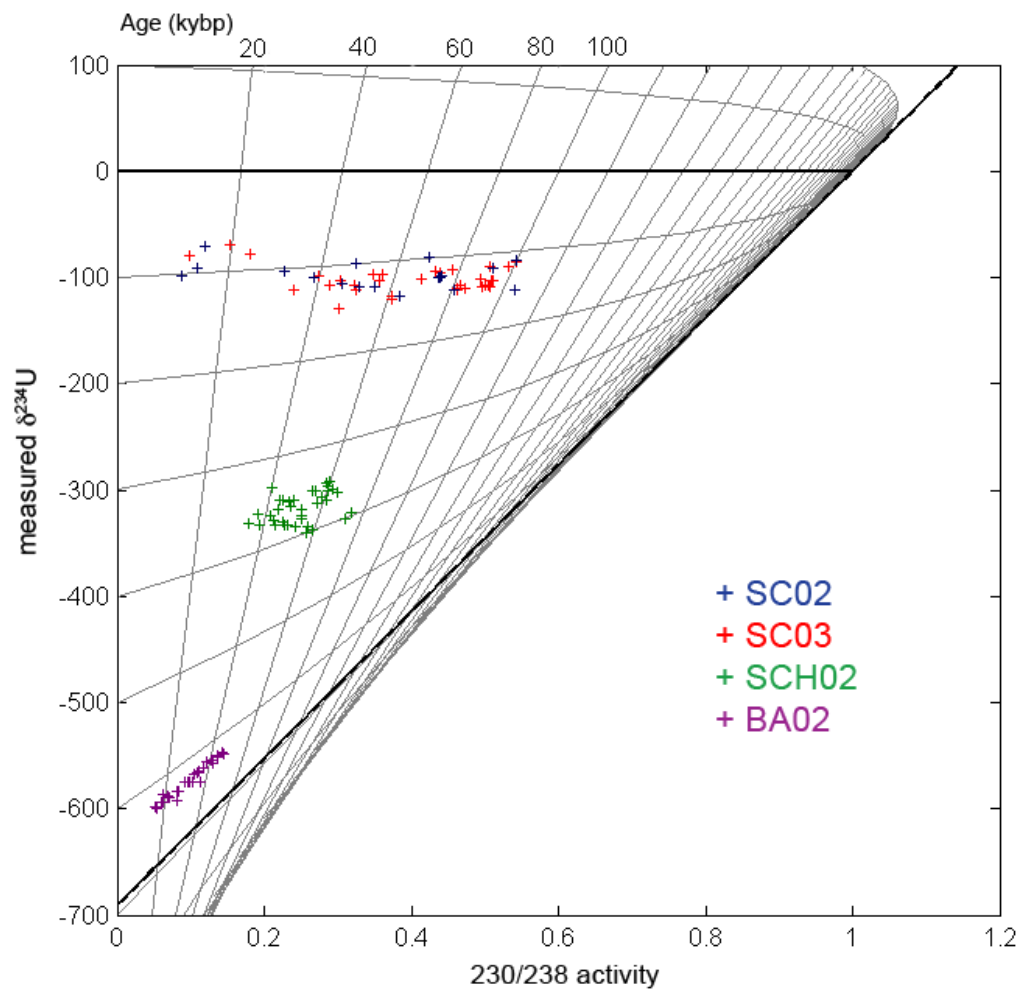


Figure S10. Diagram of the ^{238}U - ^{234}U - ^{230}Th age equation, assuming zero initial ^{230}Th . Horizontal gray contours are lines of constant initial $\delta^{234}\text{U}$, and vertical gray lines are lines of constant time, at 20 kyr intervals. The black diagonal line is the infinite age line. Measured isotopic data from all age samples (see Table S1) are plotted as ‘+’ data points – SC02 (navy), SC03 (red), SCH02 (green), and BA02 (purple).

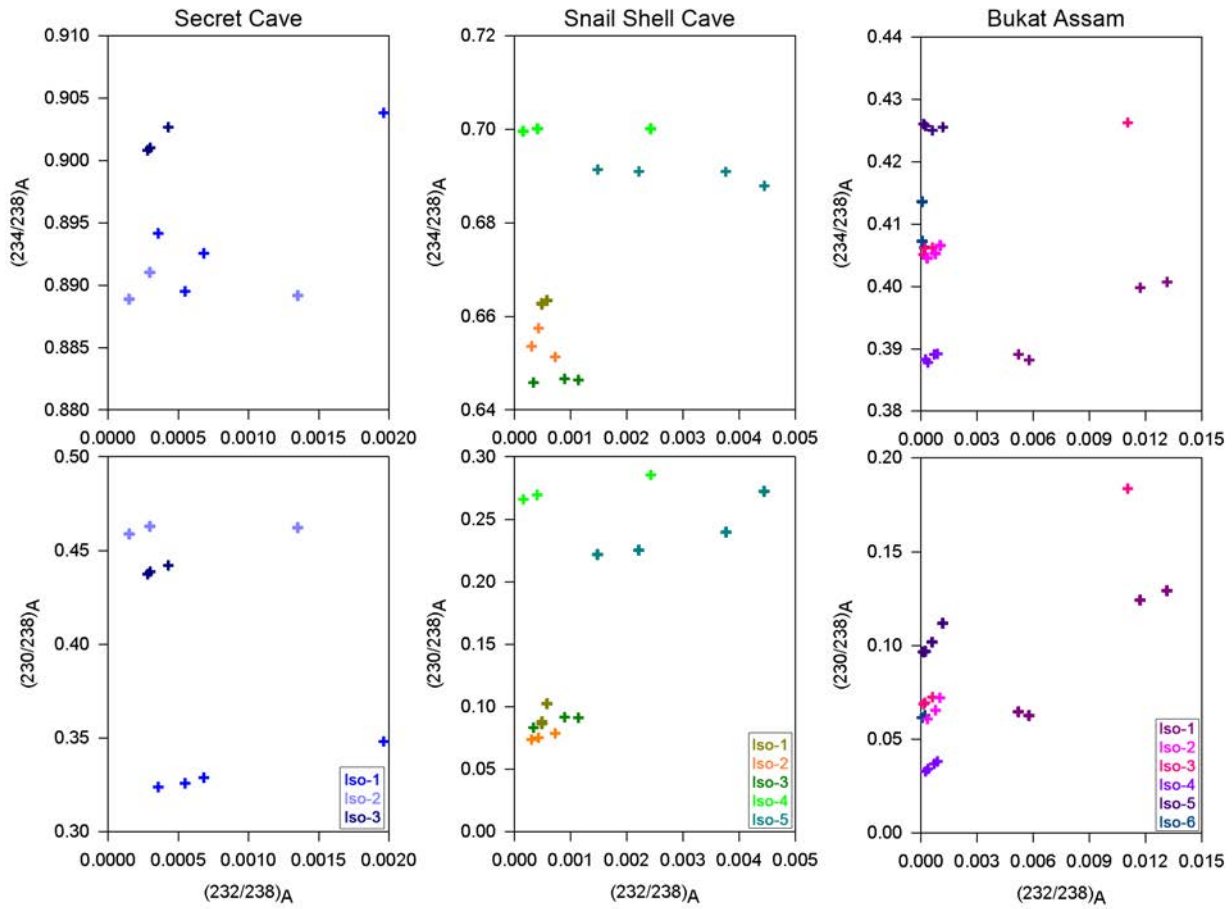


Figure S11. Osmond type isochrons for (**left**) Secret Cave at Gunung Mulu, (**middle**) Snail Shell Cave at Gunung Buda, and (**right**) Bukit Assam Cave at Gunung Buda. Colors distinguish measured isochrons at different depths (values for each listed in Table S2). Error ellipses are not shown because they are too small to be seen on this plot (see Table S2). The initial $^{230}\text{Th}/^{232}\text{Th}$ concentration is calculated using a maximum-likelihood estimation (MLE) XY-XZ isochron algorithm that finds the best line of fit to the set of XY ($^{230}\text{Th}/^{238}\text{U}$ - $^{232}\text{Th}/^{238}\text{U}$) and XZ ($^{234}\text{Th}/^{238}\text{U}$ - $^{232}\text{Th}/^{238}\text{U}$) points.

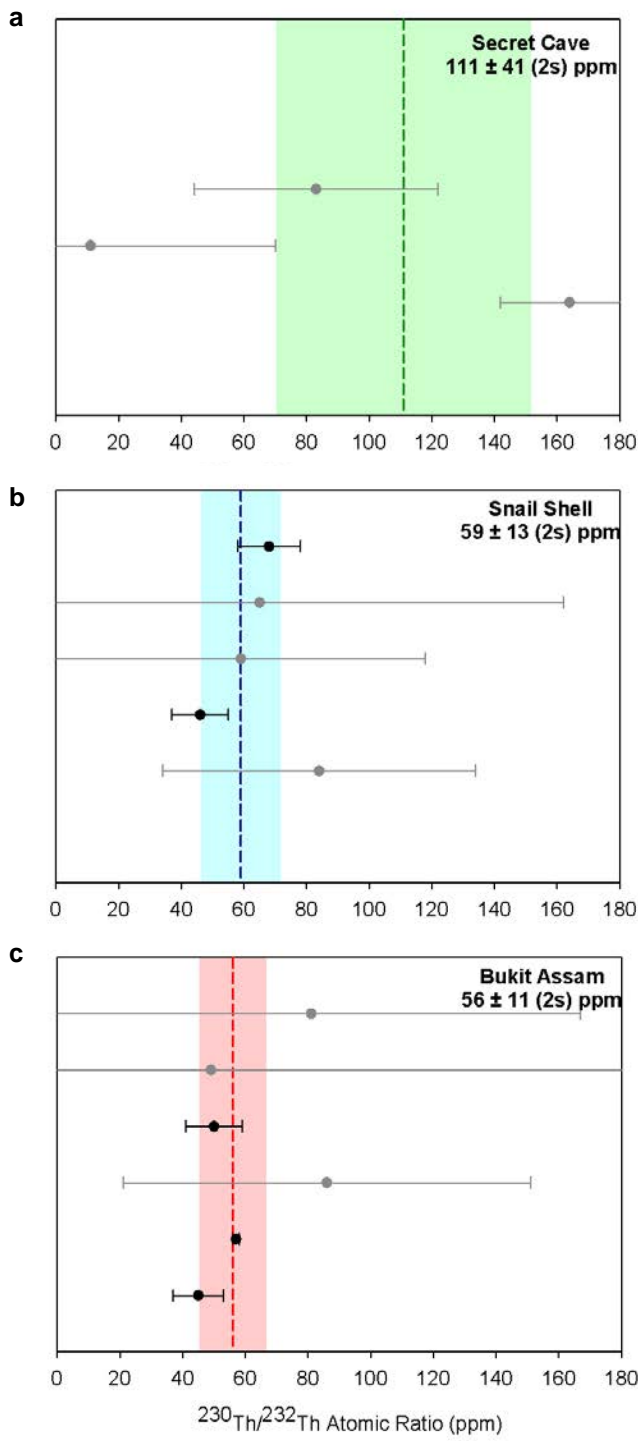


Figure S12. Plot of calculated initial $^{230}\text{Th}/^{232}\text{Th}$ concentration with 2σ error determined from each isochron, separated by cave: (a) Secret Cave (3 total), (b) Snail Shell Cave (5 total), and (c) Bukit Assam Cave (6 total). Black data points have 2σ error less than 10 ppm, gray data points have 2σ error greater than 10 ppm. Mean initial $^{230}\text{Th}/^{232}\text{Th}$ concentration plotted as colored dash line, with 2σ error shown as shaded rectangle. Note the colored 2σ error touches all black data

Table S1. Original U-Series calculated ages. Shading indicates isochrons. Data in red have been excluded from final age model (see Supp. Info.).

			MC-ICP-MS Measured Values								Uncorr	Calculated Age ^b		
Stal ID	Batch ID ^a	Core Depth (mm)	[²³⁸ U]	[²³⁸ U] error (ppb)	[²³² Th]	[²³² Th] error (pptr)	$\delta^{234}\text{U}_{(\text{T})}$	$\delta^{234}\text{U}_{(\text{T})}$ error (%)	(²³⁰ Th/ ²³⁸ U) _A	(²³⁰ Th/ ²³⁸ U) _A error	Age (kybp)	2 σ Age (kybp)	Error (-) (kyr)	Error (+) (kyr)
SC03	ce10	10	114.3	0.1	150	9.2	-79.2	0.6	0.0992	0.0008	12.47	11.41	0.41	0.41
SC03	ck15	20.5	150.6	0.1	288	2.0	-69.0	0.6	0.1539	0.0005	19.77	18.25	0.57	0.56
SC03	ck09	27	117.7	0.1	29	2.4	-78.3	0.7	0.1819	0.0007	24.09	23.89	0.13	0.13
SC03	ci09	43	167.2	0.4	147	3.3	-111.9	3.0	0.2395	0.0020	34.55	33.81	0.47	0.46
SC03	cc19	58.5	174.4	0.1	239	5.8	-99.0	0.4	0.2749	0.0008	40.05	38.91	0.45	0.45
SC03	ci19	75	107.1	0.4	158	3.5	-107.2	5.1	0.2889	0.0034	43.06	41.83	0.82	0.83
SC03	cl11	84.5	115.2	0.1	141	4.1	-103.4	0.7	0.3028	0.0004	45.41	44.38	0.39	0.39
SC03	ci01	91.5	133.6	0.4	153	3.3	-128.6	3.8	0.3022	0.0026	47.06	46.07	0.67	0.67
SC03	cc15	103.5	128.8	0.1	140	5.0	-106.6	0.5	0.3235	0.0009	49.59	48.68	0.39	0.38
SC03	cc06	103.5	143.3	0.1	239	5.5	-111.2	0.7	0.3256	0.0008	50.37	48.95	0.56	0.55
SC03	cc08	103.5	158.8	0.1	330	4.9	-108.2	1.3	0.3285	0.0007	50.72	48.96	0.67	0.69
SC03	cc04	103.5	131.7	0.1	790	5.5	-96.9	0.7	0.3478	0.0009	53.65	48.58	1.98	1.93
SC03	ck23	125	157.6	0.1	234	1.8	-102.9	0.6	0.3556	0.0005	55.76	54.52	0.49	0.48
SC03	ci06	127	119.6	0.4	216	3.5	-96.9	4.5	0.3601	0.0031	56.15	54.64	0.92	0.94
SC03	ci17	147.5	133.9	0.4	241	3.4	-118.0	4.0	0.3730	0.0028	60.94	59.39	0.95	0.95
SC03	ck07	148.5	131.5	0.1	221	2.1	-120.0	0.6	0.3728	0.0006	61.11	59.66	0.57	0.54
SC03	ci12	168	131.4	0.5	254	3.8	-101.2	4.5	0.4146	0.0032	68.53	66.90	1.10	1.08
SC03	ck03	195	140.4	0.1	203	1.9	-93.7	0.6	0.4336	0.0006	72.10	70.89	0.48	0.47
SC03	cc14	201.5	211.0	0.1	245	4.9	-95.8	0.3	0.4386	0.0006	73.57	72.60	0.39	0.39
SC03	ci16	217	130.6	0.4	188	3.3	-92.4	4.0	0.4563	0.0029	77.47	76.26	1.01	1.01
SC03	ck11	237	191.4	0.1	87	1.9	-111.8	0.5	0.4586	0.0005	80.93	80.54	0.21	0.21
SC03	ck06	237	199.5	0.1	822	2.1	-111.6	0.5	0.4622	0.0005	81.86	78.29	1.37	1.34
SC03	ck01	237	215.3	0.1	194	2.1	-109.7	0.6	0.4628	0.0005	81.73	80.96	0.32	0.33
SC03	cd22	242.5	147.0	0.1	40	29.1	-107.3	0.6	0.4670	0.0012	82.49	82.26	0.40	0.39
SC03	cd12	252.5	147.2	0.1	99	30.6	-110.8	0.5	0.4720	0.0013	84.41	83.84	0.46	0.44
SC03	ck24	266	140.7	0.1	176	1.8	-101.5	0.6	0.4937	0.0005	88.88	87.82	0.42	0.44
SC03	ck04	270	139.2	0.1	428	1.9	-89.1	0.5	0.5078	0.0006	90.67	88.09	0.98	0.97
SC03	ci14	277.5	113.4	0.4	69	3.6	-109.0	4.9	0.4953	0.0036	90.69	90.16	1.41	1.41
SC03	ck21	279.5	116.4	0.1	69	2.0	-107.1	0.6	0.5009	0.0007	92.00	91.49	0.30	0.31
SC03	ce07	293.5	163.4	0.1	83	8.0	-108.1	0.5	0.5071	0.0006	94.00	93.57	0.27	0.27
SC03	ck20	294	141.0	0.1	75	1.9	-107.7	0.6	0.5043	0.0006	93.09	92.64	0.27	0.27
SC03	ci04	301.5	159.5	0.5	38	4.1	-102.4	4.0	0.5099	0.0029	93.75	93.55	1.17	1.18
SC03	ck18	302.5	150.1	0.1	83	2.1	-102.8	0.6	0.5110	0.0007	94.14	93.67	0.28	0.28
SC03	cd11	356.5	144.9	0.1	185	32.2	-89.6	0.5	0.5325	0.0014	97.99	96.93	0.63	0.62
SC03	ck10	381.5	119.3	0.1	65	1.9	-85.7	0.6	0.5424	0.0007	100.23	99.78	0.29	0.29

^a Batch ID identifies Multi-Collector ICP-MS batch (2 letters) and sample run order within batch (1-24)

^b 2 σ errors are Monte Carlo derived, with the following initial 230/232 ratios: SCH02 = 59 ± 13 ppm; BA02 = 56 ± 11 ppm; SC03 and SC02 = 111 ± 41 ppm

Table S1. (cont'd)

			MC-ICP-MS Measured Values								Uncorr	Calculated Age ^b		
Stal ID	Batch ID ^a	Core Depth (mm)	[²³⁸ U] (ppb)	[²³⁸ U] error (ppb)	[²³² Th] (pptr)	[²³² Th] error (pptr)	$\delta^{234}\text{U}_{(\text{T})}$ (‰)	$\delta^{234}\text{U}_{(\text{T})}$ error (‰)	(²³⁰ Th/ ²³⁸ U) _A	(²³⁰ Th/ ²³⁸ U) _A error	Age (kybp)	2 σ Age (kybp)	2 σ Error (-) (kyr)	2 σ Error (+) (kyr)
SC02	cd19	274	161.2	0.1	100	30.0	-94.8	0.6	0.2283	0.0011	31.91	31.40	0.31	0.29
SC02	cd03	280	169.3	0.1	238	30.0	-99.8	0.5	0.2686	0.0010	38.97	37.80	0.51	0.47
SC02	ck13	316	153.9	0.1	354	2.1	-106.5	0.5	0.3056	0.0005	46.14	44.20	0.75	0.72
SC02	ck02	338	111.2	0.1	86	1.9	-87.3	0.6	0.3245	0.0007	48.36	47.73	0.27	0.27
SC02	ck08	343	145.0	0.1	256	2.1	-109.2	0.5	0.3286	0.0005	50.80	49.31	0.57	0.56
SC02	cd01	371.5	127.4	0.1	137	32.3	-108.6	0.6	0.3494	0.0015	54.98	54.07	0.52	0.49
SC02	cd10	388.5	162.2	0.1	154	29.0	-118.2	0.5	0.3838	0.0011	63.37	62.55	0.43	0.42
SC02	ck16	412.5	130.6	0.1	98	2.1	-80.9	1.0	0.4233	0.0007	68.17	67.55	0.30	0.30
SC02	cj15	446	205.7	0.1	174	5.0	-100.0	0.5	0.4371	0.0004	73.76	73.05	0.29	0.28
SC02	cj23	446	208.5	0.1	194	6.2	-99.7	0.6	0.4384	0.0004	74.04	73.25	0.32	0.32
SC02	cj09	446	212.7	0.1	277	5.1	-98.0	0.5	0.4418	0.0004	74.65	73.55	0.42	0.43
SC02	ce04	472.5	176.4	0.1	54	8.1	-111.6	0.5	0.4590	0.0006	81.02	80.76	0.21	0.19
SC02	cl03	478	98.4	0.1	99	4.4	-91.4	1.0	0.5116	0.0006	92.16	91.32	0.39	0.39
SC02	cl14	581	105.2	0.1	67	5.2	-84.4	0.8	0.5428	0.0006	100.10	99.57	0.31	0.32
SC02	cl05	639	148.2	0.1	14	4.6	-111.5	0.6	0.5406	0.0005	105.41	105.33	0.22	0.22

^a Batch ID identifies Multi-Collector ICP-MS batch (2 letters) and sample run order within batch (1-24)^b 2 σ errors are Monte Carlo derived, with the following initial 230/232 ratios: SCH02 = 59 ± 13 ppm; BA02 = 56 ± 11 ppm; SC03 and SC02 = 111 ± 41 ppm

Table S1. (cont'd)

			MC-ICP-MS Measured Values								Uncorr	Calculated Age ^b		
Stal ID	Batch ID ^a	Core Depth (mm)	[²³⁸ U] (ppb)	[²³⁸ U] error (ppb)	[²³² Th] (pptr)	[²³² Th] error (pptr)	$\delta^{234}\text{U}_{(\text{T})}$ (‰)	$\delta^{234}\text{U}_{(\text{T})}$ error (‰)	(²³⁰ Th/ ²³⁸ U) _A	(²³⁰ Th/ ²³⁸ U) _A error	Age (kybp)	2 σ Age (kybp)	2 σ Error (-) (kyr)	2 σ Error (+) (kyr)
SCH02	ca03	306.5	492.2	0.2	6174	3.8	-298.4	0.2	0.2109	0.0002	40.19	32.62	1.73	1.72
SCH02	cj04	318.5	598.1	0.3	7850	7.3	-317.8	0.3	0.2197	0.0002	43.96	35.71	1.87	1.87
SCH02	cj17	326.5	534.7	0.2	10510	7.4	-306.5	0.3	0.2781	0.0002	58.66	46.06	2.88	2.90
SCH02	cj14	340.5	694.5	0.3	1962	5.2	-331.3	0.3	0.1781	0.0001	34.80	33.05	0.39	0.39
SCH02	ca23	366.5	495.0	0.2	1956	11.5	-322.6	0.2	0.1906	0.0003	37.15	34.73	0.54	0.54
SCH02	ca09	393	688.9	0.3	1891	3.4	-333.6	0.2	0.1928	0.0002	38.51	36.80	0.39	0.39
SCH02	ca11	414	603.6	0.2	2758	3.2	-323.9	0.2	0.2086	0.0002	41.67	38.84	0.61	0.62
SCH02	cr04	428	603.6	0.2	1263	3.2	-312.5	0.3	0.2136	0.0004	41.97	40.30	0.38	0.38
SCH02	cr03	435	603.6	0.2	1409	2.7	-312.6	0.4	0.2147	0.0003	42.25	40.59	0.37	0.37
SCH02	ch15	441	545.5	0.2	2456	5.2	-309.1	0.3	0.2219	0.0019	43.75	41.02	0.78	0.78
SCH02	ch06	441	526.4	0.2	3551	5.6	-309.5	0.3	0.2254	0.0021	44.64	40.52	1.06	1.07
SCH02	ch19	441	510.6	0.2	6929	5.9	-312.6	0.2	0.2725	0.0019	57.84	49.18	2.09	2.02
SCH02	ch02	441	491.9	0.2	5650	6.2	-309.6	0.3	0.2398	0.0023	48.39	41.25	1.74	1.68
SCH02	ca20	457.5	640.0	0.3	1297	3.2	-328.1	0.2	0.2125	0.0002	43.02	41.76	0.29	0.28
SCH02	ca17	485	570.5	0.2	770	3.2	-332.4	0.2	0.2149	0.0002	44.05	43.20	0.20	0.20
SCH02	ca13	506.5	582.5	0.2	1382	3.4	-311.5	0.2	0.2335	0.0003	46.92	45.47	0.33	0.33
SCH02	ca24	514	590.1	0.3	1796	8.1	-316.1	0.8	0.2361	0.0004	48.07	46.19	0.44	0.43
SCH02	cj08	527.5	595.9	0.3	460	5.8	-329.5	0.3	0.2248	0.0002	46.40	45.91	0.12	0.12
SCH02	cj13	557.5	686.6	0.3	464	5.4	-332.7	0.2	0.2275	0.0002	47.43	47.00	0.11	0.11
SCH02	cj24	567	738.0	0.3	824	5.4	-332.4	0.3	0.2324	0.0001	48.73	48.03	0.16	0.16
SCH02	ca06	585	1053.7	0.4	1447	3.0	-334.6	0.2	0.2428	0.0002	51.91	51.03	0.20	0.20
SCH02	cj02	599	716.6	0.3	547	4.9	-318.3	0.3	0.2506	0.0002	52.26	51.78	0.12	0.12
SCH02	ci03	603.5	774.1	0.6	875	4.1	-324.6	0.8	0.2509	0.0005	53.05	52.34	0.24	0.24
SCH02	ca15	640	913.0	0.3	454	3.0	-327.6	0.2	0.2509	0.0002	53.41	53.10	0.09	0.09
SCH02	ca05	646	597.2	0.2	4414	4.1	-300.4	0.2	0.2857	0.0003	60.10	55.54	1.03	1.03
SCH02	ca22	646	546.5	0.2	676	3.3	-300.4	0.2	0.2693	0.0003	55.39	54.65	0.18	0.18
SCH02	ca04	646	595.3	0.2	279	3.2	-301.0	0.2	0.2661	0.0003	54.58	54.29	0.10	0.10
SCH02	cj10	670	800.0	0.3	1448	5.1	-334.0	0.2	0.2582	0.0002	56.37	55.20	0.26	0.26
SCH02	cj16	674	656.9	0.3	1186	5.0	-339.7	0.3	0.2569	0.0002	56.72	55.55	0.27	0.27
SCH02	cb07	714	991.3	0.5	1708	3.4	-337.4	0.3	0.2649	0.0003	58.87	57.74	0.27	0.26
SCH02	cb05	734	866.8	0.5	404	3.6	-293.1	0.4	0.2852	0.0002	58.97	58.69	0.11	0.11
SCH02	cb13	742	745.8	0.4	654	3.4	-292.0	0.4	0.2890	0.0005	59.91	59.39	0.19	0.19
SCH02	ci07	758	883.2	0.6	331	3.7	-295.8	0.6	0.2868	0.0004	59.78	59.56	0.16	0.16
SCH02	ci13	765	788.9	0.6	569	4.2	-310.0	0.8	0.2847	0.0006	61.10	60.65	0.22	0.23
SCH02	cb16	780	780.1	0.5	217	3.5	-299.9	0.5	0.2921	0.0002	61.91	61.74	0.10	0.11
SCH02	cb02	849	717.9	0.5	433	3.9	-301.7	0.5	0.2985	0.0003	64.11	63.74	0.15	0.14
SCH02	cb08	877	700.1	0.4	814	3.4	-327.7	0.4	0.3104	0.0004	72.41	71.65	0.24	0.23
SCH02	cb12	897	792.0	0.4	818	3.3	-321.6	0.4	0.3183	0.0005	74.03	73.36	0.23	0.24

^a Batch ID identifies Multi-Collector ICP-MS batch (2 letters) and sample run order within batch (1-24)^b 2 σ errors are Monte Carlo derived, with the following initial 230/232 ratios: SCH02 = 59 ± 13 ppm; BA02 = 56 ± 11 ppm; SC03 and SC02 = 111 ± 41 ppm

Table S1. (cont'd)

			MC-ICP-MS Measured Values								Uncorr	Calculated Age ^b		
Stal ID	Batch ID ^a	Core Depth (mm)	[²³⁸ U] (ppb)	[²³⁸ U] error (ppb)	[²³² Th] (pptr)	[²³² Th] error (pptr)	$\delta^{234}\text{U}_{(\text{T})}$ (‰)	$\delta^{234}\text{U}_{(\text{T})}$ error (‰)	(²³⁰ Th/ ²³⁸ U) _A	(²³⁰ Th/ ²³⁸ U) _A error	Age (kybp)	2 σ Age (kybp)	2 σ Error (-) (kyr)	2 σ Error (+) (kyr)
BA02	cb17	129	984.1	0.5	296	3.4	-598.4	0.2	0.0514	0.0001	15.50	15.20	0.07	0.07
BA02	cj19	147.5	1112.3	0.5	592	5.2	-600.3	0.2	0.0543	0.0001	16.55	16.02	0.11	0.11
BA02	ch10	184	1295.5	0.5	183	4.7	-586.7	0.1	0.0614	0.0008	18.29	18.15	0.25	0.26
BA02	ch18	184	1280.1	0.5	272	5.0	-593.1	0.1	0.0612	0.0008	18.57	18.36	0.29	0.29
BA02	ch16	184	1220.7	0.5	752	4.8	-594.1	0.1	0.0628	0.0008	19.16	18.55	0.31	0.31
BA02	ch03	184	1167.9	0.5	2075	5.3	-592.8	0.2	0.0811	0.0009	25.75	23.93	0.50	0.50
BA02	cb10	215	1173.6	0.6	432	3.5	-587.5	0.2	0.0686	0.0001	20.81	20.45	0.09	0.09
BA02	cb15	251	1099.6	0.5	496	3.4	-590.0	0.2	0.0717	0.0001	22.07	21.62	0.10	0.10
BA02	cb18	278	942.0	0.5	767	5.8	-583.6	0.3	0.0815	0.0001	25.16	24.36	0.17	0.17
BA02	cb01	283	943.2	0.5	779	3.5	-583.7	0.2	0.0828	0.0001	25.66	24.83	0.17	0.17
BA02	cj21	315	1249.8	0.5	552	4.7	-574.4	0.2	0.0911	0.0001	27.94	27.51	0.09	0.09
BA02	cg03	353	1192.8	0.5	492	5.8	-574.3	0.2	0.0970	0.0008	30.20	29.79	0.31	0.31
BA02	cg20	353	1194.5	0.6	817	6.7	-574.6	0.3	0.0975	0.0009	30.39	29.72	0.36	0.37
BA02	cg21	353	1272.2	0.6	2342	6.6	-575.3	0.3	0.1023	0.0008	32.35	30.50	0.48	0.49
BA02	cg09	353	1197.1	0.6	4238	7.2	-574.8	0.3	0.1124	0.0009	36.44	32.80	0.81	0.81
BA02	cb04	397.5	1228.4	0.6	446	3.6	-567.4	0.2	0.1042	0.0001	32.28	31.92	0.09	0.09
BA02	cc03	411.8	998.6	0.4	1520	5.6	-565.3	0.1	0.1093	0.0001	34.03	32.53	0.30	0.30
BA02	cc07	425.3	1092.8	0.4	1510	5.4	-564.3	0.1	0.1106	0.0001	34.46	33.10	0.27	0.27
BA02	cc13	432	986.5	0.4	840	5.5	-564.4	0.1	0.1109	0.0003	34.58	33.74	0.20	0.20
BA02	cj06	463.5	1002.0	0.5	915	5.6	-560.9	0.2	0.1175	0.0001	36.79	35.89	0.18	0.18
BA02	cc18	488	989.9	0.4	644	5.3	-556.1	0.1	0.1227	0.0001	38.34	37.70	0.13	0.14
BA02	cc10	495.5	1045.2	0.4	3593	5.4	-557.0	0.1	0.1310	0.0001	41.93	38.49	0.68	0.68
BA02	cc01	512.5	1077.2	0.4	1014	5.2	-554.9	0.1	0.1286	0.0001	40.60	39.68	0.19	0.19
BA02	cc11	516	1041.0	0.4	670	5.3	-554.6	0.1	0.1279	0.0001	40.26	39.63	0.14	0.14
BA02	cj11	539	1078.8	0.4	2014	5.0	-551.0	0.2	0.1368	0.0001	43.52	41.68	0.37	0.36
BA02	cb20	565.5	1487.8	0.7	360	4.6	-550.1	0.3	0.1366	0.0001	43.31	43.07	0.08	0.08
BA02	cj20	580	1036.6	0.4	3226	5.3	-548.3	0.2	0.1444	0.0001	46.45	43.35	0.63	0.61
BA02	cj07	595	1275.8	0.5	463	4.8	-547.4	0.1	0.1419	0.0001	45.21	44.85	0.09	0.08

^a Batch ID identifies Multi-Collector ICP-MS batch (2 letters) and sample run order within batch (1-24)^b 2 σ errors are Monte Carlo derived, with the following initial 230/232 ratios: SCH02 = 59 ± 13 ppm; BA02 = 56 ± 11 ppm; SC03 and SC02 = 111 ± 41 ppm

Table S2. Osmond-type activity ratios used in isochron calculations. Plotted in Figure S12 by cave type.

Cave	Stal ID	Isochron No.	Batch ID	(232/ 238) _A	2σ error	(230/ 238) _A	2σ error	(234/ 238) _A	2σ error
Bukat Assam	BA04	Iso-1	sc02	5.21E-03	6.12E-06	6.47E-02	4.02E-04	3.89E-01	3.26E-04
	BA04		sc03	5.77E-03	8.21E-06	6.25E-02	3.23E-04	3.88E-01	2.80E-04
	BA04		sc04	1.17E-02	1.46E-05	1.24E-01	3.25E-04	4.00E-01	2.60E-04
	BA04		sc05	1.32E-02	1.87E-05	1.29E-01	4.79E-04	4.01E-01	2.17E-04
	BA04	Iso-2	sd06	3.38E-04	1.09E-07	6.06E-02	1.33E-04	4.05E-01	8.22E-04
	BA04		sd07	7.66E-04	3.10E-07	6.54E-02	1.66E-04	4.05E-01	8.79E-04
	BA04		sd08	1.01E-03	3.08E-07	7.21E-02	1.57E-04	4.07E-01	8.59E-04
	BA04	Iso-3	sc09	1.10E-02	8.48E-06	1.84E-01	2.48E-04	4.26E-01	1.85E-04
	BA04		sc10	6.18E-04	6.37E-07	7.23E-02	2.17E-04	4.06E-01	2.06E-04
	BA04		sc11	1.39E-04	3.20E-07	6.88E-02	2.23E-04	4.05E-01	2.24E-04
	BA04		sc12	1.91E-04	4.25E-07	6.94E-02	2.68E-04	4.06E-01	2.07E-04
	BA04	Iso-4	sg20	6.92E-04	8.46E-07	3.68E-02	7.05E-05	3.89E-01	1.47E-04
	BA04		sg23	2.51E-04	8.19E-07	3.27E-02	7.01E-05	3.88E-01	1.54E-04
	BA04		sg36	3.59E-04	7.70E-07	3.39E-02	6.47E-05	3.88E-01	1.58E-04
	BA04		sg15	8.89E-04	1.15E-06	3.80E-02	8.85E-05	3.89E-01	1.65E-04
	BA02	Iso-5	cg03*	1.35E-04	2.02E-06	9.65E-02	3.51E-03	4.26E-01	2.48E-04
	BA02		cg20*	2.24E-04	2.30E-06	9.69E-02	3.99E-03	4.26E-01	2.71E-04
	BA02		cg21*	6.03E-04	2.14E-06	1.02E-01	3.69E-03	4.25E-01	2.63E-04
	BA02	Iso-6	ch10*	4.62E-05	1.18E-06	6.15E-02	7.55E-04	4.14E-01	1.46E-04
	BA02		ch18*	6.95E-05	1.28E-06	6.13E-02	8.18E-04	4.07E-01	1.43E-04
	BA02		ch16*	2.02E-04	1.28E-06	6.28E-02	8.21E-04	4.06E-01	1.39E-04
Snail Shell	SCH02	Iso-1	se17	1.81E-04	7.14E-07	8.79E-02	1.20E-04	6.63E-01	2.07E-04
	SCH02		se18	1.24E-04	6.55E-07	8.63E-02	1.07E-04	6.63E-01	1.95E-04
	SCH02		se19	1.40E-03	8.83E-07	1.03E-01	1.16E-04	6.63E-01	2.35E-04
	SCH02	Iso-2	se20	7.19E-04	8.67E-07	7.87E-02	1.38E-04	6.51E-01	2.68E-04
	SCH02		se21	3.05E-04	7.19E-07	7.39E-02	9.99E-05	6.54E-01	2.25E-04
	SCH02		se22	4.30E-04	7.48E-07	7.53E-02	1.08E-04	6.58E-01	2.67E-04
	SCH02	Iso-3	se23	1.14E-03	5.59E-07	9.13E-02	8.77E-05	6.46E-01	1.97E-04
	SCH02		se24	3.38E-04	4.44E-07	8.32E-02	8.46E-05	6.46E-01	2.20E-04
	SCH02		se25	8.89E-04	4.81E-07	9.15E-02	8.58E-05	6.47E-01	2.34E-04
	SCH02	Iso-4	ca05*	2.42E-03	2.03E-06	2.86E-01	3.28E-04	7.00E-01	2.30E-04
	SCH02		ca22*	4.05E-04	1.96E-06	2.70E-01	3.19E-04	7.00E-01	2.02E-04
	SCH02		ca04*	1.54E-04	1.76E-06	2.66E-01	3.14E-04	7.00E-01	2.38E-04
	SCH02	Iso-5	ch15*	1.48E-03	3.05E-06	2.22E-01	1.92E-03	6.91E-01	2.78E-04
	SCH02		ch06*	2.21E-03	3.34E-06	2.26E-01	2.07E-03	6.91E-01	2.59E-04
	SCH02		ch19*	4.45E-03	1.01E-05	2.73E-01	2.03E-03	6.88E-01	2.71E-03
	SCH02		ch02*	3.76E-03	3.78E-06	2.40E-01	2.29E-03	6.91E-01	3.12E-04
Secret	SC03	Iso-1	cc15*	3.56E-04	1.27E-05	3.24E-01	8.55E-04	8.94E-01	5.36E-04
	SC03		cc06*	5.48E-04	1.27E-05	3.26E-01	8.49E-04	8.90E-01	6.51E-04
	SC03		cc08*	6.81E-04	1.01E-05	3.29E-01	7.19E-04	8.93E-01	1.27E-03
	SC03		cc04*	1.96E-03	1.38E-05	3.48E-01	9.18E-04	9.04E-01	6.66E-04
	SC03	Iso-2	cc15*	1.49E-04	3.31E-06	4.59E-01	4.83E-04	8.89E-01	4.86E-04
	SC03		cc06*	1.35E-03	3.39E-06	4.62E-01	5.05E-04	8.89E-01	4.81E-04
	SC03		cc08*	2.96E-04	3.18E-06	4.63E-01	4.50E-04	8.91E-01	5.78E-04
	SC02	Iso-3	cc15*	2.77E-04	7.95E-06	4.37E-01	3.94E-04	9.01E-01	5.41E-04
	SC02		cc06*	3.04E-04	9.72E-06	4.39E-01	4.14E-04	9.01E-01	5.98E-04
	SC02		cc08*	4.27E-04	7.83E-06	4.42E-01	3.90E-04	9.03E-01	5.31E-04

(*) indicates new isochrons not previously published.

Table S3. Calculation of detrital 230/232 concentration for each cave system (BA02 and BA04; SCH02; SSC01; and SC03). Final detrital 230/232 concentration used for each stalagmite is: BA02 = 56 ± 11 ppm; SCH02 = 59 ± 13 ppm; SC03 and SC02 = 111 ± 41 ppm (see Supp. Info.).

		Osmond Type ^b								Weight ^c	Detrital 230/232 (ppm)			
Stal ID	Isochron ^a	Age (kyr)	2 σ error (kyr)	(230/238) _A Intercept	2 σ error	(234/238) _A Intercept	2 σ error	Detrital 230/232 (ppm)	2 σ error (ppm)		Wtd Mean	Wtd 2 σ ^d	Un-wtd Mean	Un-wtd 2 σ ^e
BA04	Iso-1	3.6	4.5	0.0120	0.0150	0.3800	0.0110	50	9	0.2313	56	1	62	35
	Iso-2	16.5	3.7	0.0547	0.0083	0.4040	0.0510	86	65	0.0308				
	Iso-3	20.5	0.5	0.0667	0.0013	0.4052	0.0011	57	1	1.4800				
	Iso-4	9.2	0.3	0.0308	0.0008	0.3875	0.0017	45	8	0.2643				
	Iso-5*	28.8	4.1	0.0940	0.0110	0.4258	0.0008	81	86	0.0231				
	Iso-6*	18.0	23.0	0.0610	0.0670	0.4130	0.0130	49	2973	0.0007				
SCH02	Iso-1	15.1	0.3	0.0852	0.0015	0.6626	0.0027	68	10	0.1947	59	4	64	27
	Iso-2	12.4	1.7	0.0703	0.0085	0.6570	0.0180	65	97	0.0206				
	Iso-3	14.6	2.0	0.0800	0.0095	0.6460	0.0240	59	59	0.0336				
	Iso-4*	54.1	0.7	0.2656	0.0024	0.6999	0.0017	46	9	0.2313				
	Iso-5*	37.0	6.8	0.1950	0.0290	0.6917	0.0050	84	50	0.0398				
SC03	Iso-1*	48.7	1.5	0.3181	0.0074	0.8892	0.0056	83	39	0.0507	111	11	86	153
	Iso-2*	80.9	2.6	0.4607	0.0084	0.8898	0.0092	11	59	0.0336				
SC02	Iso-3*	71.9	0.4	0.4293	0.0014	0.8970	0.0017	164	22	0.0925				

^a (*) indicates new isochrons not previously published.

^b Age, intercepts, and detrital 230/232 calculated using ISOPLOT 3.72 (Ludwig, 1993). The 230/238 and 234/238 intercepts are the Y-Z plane intercepts of the linear 3-D isochron used to calculate an age and initial 234/238 using X = 232/238, Y = 230/238, Z = 234/238 (Ludwig and Titterington, 1994).

^c Weights calculated as inverse of 1 standard deviation of the detrital 230/232 for each isochron.

^d Weighted standard deviation is the inverse of the sum of the weights for each cave system.

^e Un-weighted standard deviation is the standard deviation of the n-isochron 230/232 for each cave system.

Table S4. Adjusted age model for SC03, SC02, SCH02, and BA02 used in Figures 2. Adjusted age is within limits in all cases.

Stal ID	Batch ID	Core Depth (mm)	Lower Age (2s) ^a (ybp)	Original Age ^a (ybp)	Adjusted Age (ybp)	Upper Age (2s) ^a (ybp)	Growth Rate ^b (year/mm)
SC03	ck09	27	23,758	23,889	23,889	24,017	
SC03	ci09	43	33,343	33,811	33,811	34,267	--hiatus--
SC03	cc19	58.5	38,462	38,910	38,910	39,356	329
SC03	ci19	75	41,007	41,828	41,828	42,656	177
SC03	cl11	84.5	43,992	44,381	44,381	44,773	269
SC03	ci01	91.5	45,406	46,075	46,075	46,749	242
SC03	cc15	103.5	48,294	48,679	48,679	49,058	217
SC03	ck23	125	54,030	54,515	54,515	55,000	271
SC03	ck07	148.5	59,092	59,657	59,657	60,200	219
SC03	ci12	168	65,803	66,898	66,898	67,976	371
SC03	ck03	195	70,417	70,893	71,353	71,359	165
SC03	cc14	201.5	72,213	72,602	72,902	72,988	238
SC03	ci16	217	75,258	76,265	76,265	77,271	217
SC03	ck11	237	80,338	80,543	80,543	80,749	214
SC03	cd22	242.5	81,863	82,261	82,261	82,651	312
SC03	cd12	252.5	83,375	83,835	83,835	84,275	157
SC03	ck24	266	87,404	87,823	87,523	88,261	273
SC03	ck04	270	87,113	88,092	88,592	89,059	267
SC03	ck21	279.5	91,188	91,491	91,391	91,803	295
SC03	ck20	294	92,368	92,637	92,837	92,907	100
SC03	ck18	302.5	93,389	93,673	93,673	93,957	98
SC03	cd11	356.5	96,300	96,926	97,326	97,542	68
SC03	ck10	381.5	99,482	99,776	99,776	100,069	98
SC02	cd03	280	37,290	37,799	37,799	38,274	
SC02	ck13	316	43,451	44,198	44,198	44,916	178
SC02	ck02	338	47,461	47,731	47,731	47,997	161
SC02	ck08	343	48,741	49,309	49,309	49,868	316
SC02	cd01	371.5	53,544	54,068	54,068	54,554	167
SC02	cd10	388.5	62,119	62,552	62,552	62,972	169/ hiatus/ 214
SC02	ck16	412.5	67,256	67,554	67,554	67,851	208
SC02	cj15	446	72,760	73,054	73,054	73,339	164
SC02	ce04	472.5	80,549	80,758	80,758	80,951	194 / hiatus
SC02	cl03	478	90,935	91,322	91,322	91,709	hiatus / 80
SC02	cl14	581	99,257	99,569	99,569	99,887	80
SC02	cl05	639	105,115	105,333	105,333	105,551	99

^a Original calculated age with upper and lower limits (95% confidence interval calculated using Monte Carlo simulation)

^b Linear growth rates for each interval between 2 consecutive U-series dates that do not include a hiatus. If a hiatus exists between two U-series dates, growth rate was assigned the same growth rate as adjacent age models either above or below (use of linear extrapolation)

Table S4. (cont'd)

Stal ID	Batch ID	Core Depth (mm)	Lower Age (2s) ^a (ybp)	Original Age ^a (ybp)	Adjusted Age (ybp)	Upper Age (2s) ^a (ybp)	Growth Rate ^b (year/mm)
SCH02	cj14	340.5	32,666	33,052	32,852	33,440	
SCH02	ca23	366.5	34,185	34,729	34,529	35,268	64
SCH02	ca09	393	36,408	36,797	36,497	37,182	74
SCH02	ca11	414	38,226	38,837	38,537	39,455	97
SCH02	cr04	428	39,923	40,298	39,998	40,681	104
SCH03	cr03	435	40,226	40,591	40,291	40,958	42
SCH02	ch15	441	40,234	41,017	40,417	41,794	21
SCH02	ca20	457.5	41,466	41,759	41,759	42,042	81
SCH02	ca17	485	43,008	43,205	43,205	43,401	53
SCH02	ca13	506.5	45,143	45,471	45,471	45,797	105
SCH02	cj08	527.5	45,790	45,913	45,913	46,036	21
SCH02	cj13	557.5	46,891	47,004	47,004	47,112	36
SCH02	cj24	567	47,863	48,026	47,926	48,190	97
SCH02	ca06	585	50,838	51,034	51,034	51,235	--hiatus--
SCH02	cj02	599	51,664	51,782	51,782	51,901	53
SCH02	ci03	603.5	52,105	52,343	52,113	52,579	74
SCH02	ca15	640	53,007	53,098	53,098	53,187	27
SCH02	ca04	646	54,193	54,293	54,293	54,391	--hiatus--
SCH02	cj10	670	54,940	55,204	55,204	55,465	38
SCH02	cj16	674	55,281	55,547	55,547	55,818	86
SCH02	cb07	714	57,476	57,743	57,743	58,004	55
SCH02	cb05	734	58,581	58,691	58,691	58,798	47
SCH02	cb13	742	59,201	59,388	59,208	59,574	65
SCH02	ci07	758	59,393	59,556	59,716	59,718	32
SCH02	ci13	765	60,428	60,652	60,432	60,880	102
SCH02	cb16	780	61,635	61,740	61,640	61,845	81
SCH02	cb02	849	63,597	63,742	63,887	63,887	33
SCH02	cb08	877	71,412	71,649	71,649	71,879	--hiatus--
SCH02	cb12	897	73,127	73,359	73,359	73,594	86
BA02	cb17	129	15,135	15,200	15,200	15,268	
BA02	cj19	147.5	15,912	16,020	16,020	16,126	44
BA02	ch10	184	17,900	18,153	18,153	18,411	58
BA02	cb10	215	20,364	20,450	20,450	20,537	74
BA02	cb15	251	21,524	21,622	21,622	21,718	33
BA02	cb18	278	24,189	24,355	24,355	24,525	101
BA02	cb01	283	24,668	24,833	24,833	25,005	96
BA02	cj21	315	27,422	27,511	27,511	27,600	84
BA02	cg03	353	29,478	29,792	29,792	30,101	60
BA02	cb04	397.5	31,836	31,925	31,925	32,013	48
BA02	cc03	411.8	32,233	32,533	32,533	32,833	43
BA02	cc07	425.3	32,833	33,104	33,104	33,377	42
BA02	cc13	432	33,539	33,742	33,742	33,942	95
BA02	cj06	463.5	35,710	35,894	35,894	36,074	68
BA02	cc18	488	37,571	37,704	37,704	37,842	74
BA02	cc10	495.5	37,812	38,492	38,492	39,171	105
BA02	cc01	512.5	39,484	39,677	39,527	39,870	61
BA02	cc11	516	39,495	39,631	39,761	39,771	67
BA02	cj11	539	41,307	41,679	41,679	42,040	83
BA02	cb20	565.5	42,997	43,075	43,075	43,152	53
BA02	cj20	580	42,723	43,348	43,748	43,954	46
BA02	cj07	595	44,768	44,853	44,853	44,936	74

^a Original calculated age with upper and lower limits (95% confidence interval calculated using Monte Carlo simulation)

^b Linear growth rates for each interval between 2 consecutive U-series dates that do not include a hiatus. If a hiatus exists between two U-series dates, growth rate was assigned the same growth rate as adjacent age models either above or below (use of linear extrapolation)

References and Notes

1. Y. J. Wang *et al.*, A high-resolution absolute-dated late Pleistocene Monsoon record from Hulu Cave, China. *Science* **294**, 2345 (2001). [doi:10.1126/science.1064618](https://doi.org/10.1126/science.1064618)
2. Y. J. Wang *et al.*, Millennial- and orbital-scale changes in the East Asian monsoon over the past 224,000 years. *Nature* **451**, 1090 (2008). [doi:10.1038/nature06692](https://doi.org/10.1038/nature06692) Medline
3. W. Dansgaard *et al.*, Evidence for general instability of past climate from a 250-kyr ice-core record. *Nature* **364**, 218 (1993). [doi:10.1038/364218a0](https://doi.org/10.1038/364218a0)
4. H. Heinrich, Origin and consequences of cyclic ice rafting in the northeast Atlantic-ocean during the past 130,000 years. *Quat. Res.* **29**, 142 (1988). [doi:10.1016/0033-5894\(88\)90057-9](https://doi.org/10.1016/0033-5894(88)90057-9)
5. S. R. Hemming, Heinrich events: Massive late pleistocene detritus layers of the North Atlantic and their global climate imprint. *Rev. Geophys.* **42**, RG1005 (2004). [doi:10.1029/2003RG000128](https://doi.org/10.1029/2003RG000128)
6. J. W. Partin, K. M. Cobb, J. F. Adkins, B. Clark, D. P. Fernandez, Millennial-scale trends in west Pacific warm pool hydrology since the Last Glacial Maximum. *Nature* **449**, 452 (2007). [doi:10.1038/nature06164](https://doi.org/10.1038/nature06164) Medline
7. M. R. Cane, A. C. Clement, A role for the tropical Pacific coupled ocean-atmosphere system on Milankovich and millennial timescales. *Geophys. Monogr.* **112**, 373 (1999). [doi:10.1029/GM112p0373](https://doi.org/10.1029/GM112p0373)
8. Materials and methods are available as supplementary materials on *Science* Online.
9. D. Scholz, D. L. Hoffmann, StalAge – An algorithm designed for construction of speleothem age models. *Quat. Geochronol.* **6**, 369 (2011). [doi:10.1016/j.quageo.2011.02.002](https://doi.org/10.1016/j.quageo.2011.02.002)
10. J. W. Moerman *et al.*, Diurnal to interannual rainfall $\delta^{18}\text{O}$ variations in northern Borneo driven by regional hydrology. *Earth Planet. Sci. Lett.* **369-370**, 108 (2013). [doi:10.1016/j.epsl.2013.03.014](https://doi.org/10.1016/j.epsl.2013.03.014)
11. W. Dansgaard, Stable isotopes in precipitation. *Tellus* **16**, 436 (1964). [doi:10.1111/j.2153-3490.1964.tb00181.x](https://doi.org/10.1111/j.2153-3490.1964.tb00181.x)
12. K. Rozanski, L. Araguás-Araguás, R. Gonfiantini, Relation between long-term trends of oxygen-18 isotope composition of precipitation and climate. *Science* **258**, 981 (1992). [doi:10.1126/science.258.5084.981](https://doi.org/10.1126/science.258.5084.981)
13. K. M. Cobb, J. F. Adkins, J. W. Partin, B. Clark, Regional-scale climate influences on temporal variations of rainwater and cave dripwater oxygen isotopes in northern Borneo. *Earth Planet. Sci. Lett.* **263**, 207 (2007). [doi:10.1016/j.epsl.2007.08.024](https://doi.org/10.1016/j.epsl.2007.08.024)
14. A. N. Meckler, M. O. Clarkson, K. M. Cobb, H. Sodemann, J. F. Adkins, Interglacial hydroclimate in the tropical West Pacific through the Late Pleistocene. *Science* **336**, 1301 (2012). [doi:10.1126/science.1218340](https://doi.org/10.1126/science.1218340)
15. C. Waelbroeck *et al.*, Sea-level and deep water temperature changes derived from benthic foraminifera isotopic records. *Quat. Sci. Rev.* **21**, 295 (2002). [doi:10.1016/S0277-3791\(01\)00101-9](https://doi.org/10.1016/S0277-3791(01)00101-9)

16. M. Zhao, C.-Y. Huang, C.-C. Wang, G. Wei, A millennial-scale U_{37}^K sea-surface temperature record from the South China Sea (8°N) over the last 150 kyr: Monsoon and sea-level influence. *Palaeogeogr. Palaeoclimatol. Palaeoecol.* **236**, 39 (2006). [doi:10.1016/j.palaeo.2005.11.033](https://doi.org/10.1016/j.palaeo.2005.11.033)
17. D. W. Oppo, Y. B. Sun, Amplitude and timing of sea-surface temperature change in the northern South China Sea: Dynamic link to the East Asian monsoon. *Geology* **33**, 785 (2005). [doi:10.1130/G21867.1](https://doi.org/10.1130/G21867.1)
18. A. B. G. Bush, R. G. Fairbanks, Exposing the Sunda shelf: Tropical responses to eustatic sea level change. *J. Geophys. Res. D Atmos.* **108**, 4446 (2003). [doi:10.1029/2002JD003027](https://doi.org/10.1029/2002JD003027)
19. P. N. DiNezio *et al.*, The response of the Walker circulation to Last Glacial Maximum forcing: Implications for detection in proxies. *Paleoceanography* **26**, PA3217 (2011). [doi:10.1029/2010PA002083](https://doi.org/10.1029/2010PA002083)
20. K. B. Cutler *et al.*, Rapid sea-level fall and deep-ocean temperature change since the last interglacial period. *Earth Planet. Sci. Lett.* **206**, 253 (2003). [doi:10.1016/S0012-821X\(02\)01107-X](https://doi.org/10.1016/S0012-821X(02)01107-X)
21. P. De Deckker, N. J. Tapper, S. Van der Kaars, The status of the Indo-Pacific Warm Pool and adjacent land at the Last Glacial Maximum. *Global Planet. Change* **35**, 25 (2002). [doi:10.1016/S0921-8181\(02\)00089-9](https://doi.org/10.1016/S0921-8181(02)00089-9)
22. J. E. Tierney *et al.*, The influence of Indian Ocean atmospheric circulation on Warm Pool hydroclimate during the Holocene epoch. *J. Geophys. Res. D Atmos.* **117**, D19108 (2012). [doi:10.1029/2012JD018060](https://doi.org/10.1029/2012JD018060)
23. R. A. Madden, P. R. Julian, Description of global-scale circulation cells in tropics with a 40–50 day period. *J. Atmos. Sci.* **29**, 1109 (1972). [doi:10.1175/1520-0469\(1972\)029<1109:DOGSCC>2.0.CO;2](https://doi.org/10.1175/1520-0469(1972)029<1109:DOGSCC>2.0.CO;2)
24. S. Dannenmann, B. K. Linsley, D. W. Oppo, Y. Rosenthal, L. Beaufort, East Asian monsoon forcing of suborbital variability in the Sulu Sea during Marine Isotope Stage 3: Link to Northern Hemisphere climate. *Geochem. Geophys. Geosyst.* **4**, 1 (2003). [doi:10.1029/2002GC000390](https://doi.org/10.1029/2002GC000390)
25. R. Zhang, T. L. Delworth, Simulated tropical response to a substantial weakening of the Atlantic thermohaline circulation. *J. Clim.* **18**, 1853 (2005). [doi:10.1175/JCLI3460.1](https://doi.org/10.1175/JCLI3460.1)
26. J. C. H. Chiang, C. M. Bitz, Influence of high latitude ice cover on the marine Intertropical Convergence Zone. *Clim. Dyn.* **25**, 477 (2005). [doi:10.1007/s00382-005-0040-5](https://doi.org/10.1007/s00382-005-0040-5)
27. L. C. Kanner, S. J. Burns, H. Cheng, R. L. Edwards, High-latitude forcing of the South American summer monsoon during the Last Glacial. *Science* **335**, 570 (2012). [doi:10.1126/science.1213397](https://doi.org/10.1126/science.1213397)
28. C. Barbante *et al.*; EPICA Community Members, One-to-one coupling of glacial climate variability in Greenland and Antarctica. *Nature* **444**, 195 (2006). [doi:10.1038/nature05301](https://doi.org/10.1038/nature05301) [Medline](#)
29. H. Rashid, R. Hesse, D. J. W. Piper, Evidence for an additional Heinrich event between H5 and H6 in the Labrador Sea. *Paleoceanography* **18**, 1077 (2003). [doi:10.1029/2003PA000913](https://doi.org/10.1029/2003PA000913)

30. M. Storey, R. G. Roberts, M. Saidin, Astronomically calibrated $^{40}\text{Ar}/^{39}\text{Ar}$ age for the Toba supereruption and global synchronization of late Quaternary records. *Proc. Natl. Acad. Sci. U.S.A.* **109**, 18684 (2012). [doi:10.1073/pnas.1208178109](https://doi.org/10.1073/pnas.1208178109) [Medline](#)
31. K. K. Andersen *et al.*; North Greenland Ice Core Project members, High-resolution record of Northern Hemisphere climate extending into the last interglacial period. *Nature* **431**, 147 (2004). [doi:10.1038/nature02805](https://doi.org/10.1038/nature02805) [Medline](#)
32. E. W. Wolff, J. Chappellaz, T. Blunier, S. O. Rasmussen, A. Svensson, Millennial-scale variability during the last glacial: The ice core record. *Quat. Sci. Rev.* **29**, 2828 (2010). [doi:10.1016/j.quascirev.2009.10.013](https://doi.org/10.1016/j.quascirev.2009.10.013)
33. A. Berger, M. F. Loutre, Insolation values for the climate of the last 10 million years. *Quat. Sci. Rev.* **10**, 297 (1991). [doi:10.1016/0277-3791\(91\)90033-Q](https://doi.org/10.1016/0277-3791(91)90033-Q)
34. E. Bard, B. Hamelin, R. G. Fairbanks, A. Zindler, Calibration of the C-14 timescale over the past 30,000 years using mass-spectrometric U-Th ages from Barbados corals. *Nature* **345**, 405 (1990). [doi:10.1038/345405a0](https://doi.org/10.1038/345405a0)
35. E. Bard, B. Hamelin, R. G. Fairbanks, U-Th ages obtained by mass-spectrometry in corals from Barbados: Sea-level during the past 130,000 years. *Nature* **346**, 456 (1990). [doi:10.1038/346456a0](https://doi.org/10.1038/346456a0)
36. K. R. Ludwig, D. M. Titterington, Calculation of $^{230}\text{Th}/\text{U}$ isochrons, ages, and errors. *Geochim. Cosmochim. Acta* **58**, 5031 (1994). [doi:10.1016/0016-7037\(94\)90229-1](https://doi.org/10.1016/0016-7037(94)90229-1)
37. K. R. Ludwig, UISO-A program for calculation of ^{230}Th - ^{234}U - ^{238}U isochrons. *USGS Open File Report* **93-531** (1993).
38. L. Stott, C. Poulsen, S. Lund, R. Thunell, Super ENSO and global climate oscillations at millennial time scales. *Science* **297**, 222 (2002). [doi:10.1126/science.1071627](https://doi.org/10.1126/science.1071627)